Dynamic Analysis of the Ampelmann G25 Gangway

by

Yiu Cho Chung

to obtain the degree of Master of Science
at the Delft University of Technology.

Student number:	1397761	
Date:	June 2016	
Thesis committee:	Prof. dr. ir. A. Metrikine,	TU Delft, Chairman
	Dr. K. van Dalen,	TU Delft, Supervisor
	Ir. J.S. Hoving,	TU Delft, Supervisor
	PhD T. Lu,	TU Delft, Supervisor
	Dr. M. Gutiérrez,	Ampelmann B.V.
	Ir. A. Ronse,	Ampelmann B.V.

TU Delft Delft University of Technology

AMPELMANN

Acknowledgement

I would like to express my sincere gratitude to Prof. Andrei Metrikine, Chairman of the Graduation Committee who gave me the opportunity to graduate under his supervision.
This project has been made possible by the company Ampelmann Operations B.V. Hereby, I would like to thank Alexander Ronse and Miguel Gutiérrez for giving me this opportunity and for supervising me during the research.
I would also like to thank faculty members Dr.Karel van Dalen and Tao Lu for their great support for steering me in the right direction.

Without their support and input, I could not have completed my research successfully. I am grateful for their valuable comments on my thesis.

Yiu Cho Chung
Delft, June 2016

Abstract

The Ampelmann system is an active motion compensation system that can compensate the vessel motions in six degrees of freedom. The Ampelmann, together with the attached gangway, makes it possible for people to transfer between a vessel and offshore structures safely. The Ampelmann system has been designed in the early stages based on a set of static load cases.
For design and analysis related to fatigue life estimation, system operability and control improvements, it is necessary to obtain more insights in the structural dynamics of the system. With the earliest system approaching a lifetime of 10 years, fatigue lifetime is of high importance and forms the main goal of this study.

The main function of the Ampelmann gangway is to serve as a bridge for people transfer between the ship, where the Ampelmann system is placed on board, and the offshore structure. Ampelann utilize various types of gangways in the market. This thesis focus primarily on the most widely used gangway (G25), which consist of a Main Boom and a telescoping T-boom. The transfer deck in which gangway is attached to is assumed to be rigid. To asses G25 for fatigue, first dynamic behavior under certain loading must be determined. In general the gangway in operation experiences various load conditions, which have to be taken into account. However, in this only the load condition under steady wind velocity, base excitation and rotation of the gangway under applied torque is considered.

The gangway is modeled as a step or segmented Euler-Bernoulli beam to describe the dynamic characteristic of the gangway itself. The dynamic characteristics are the mode shape and natural frequency in its vibrating plane. Since the gangway is a 'U' shape like beam, the offset of the shear center will cause coupled effect between bending and torsion in its relevant vibrating plane. A one dimensional Finite Element Beam model is implemented to determine the structural vibration characteristic and the dynamic behavior under external loading.

From experimental data the damping ratio was determined and the free vibration decay between the one dimensional model and experiment was compared. It was found that the period and the static deflection of the model is slightly higher than experimental data. The dynamic behavior of the gangway under constant wind velocity was investigated. The results show that for high wind velocity the gangway is highly damped due to the aerodynamic damping in the model and also appears that bending displacement damped out faster than the torsional displacement.

Two models were used to describe the dynamics of the gangway under base excitation, the first one being a sinusoidal model and the second model being a pulse excitation. The sinusoidal model is used to describe when the Ampelmann system is in non-compensation mode where the base dynamics are dominated by wave-induced vessel motions, while pulse excitation describes the system in compensation mode where the dynamics are dominated by the hexapod reaching its work space limits. No coupled motion is expected in this case since the shear center lies on the vibrating axis. The results in sinusoidal model shows that the steady state is rapidly reached and less abrupt oscillation is observed when compare to the pulse excitation model.

Vibration of the gangway during operational cycle (Luffing, Slewing and Telescoping) were also investigated without the wind loads and base excitation and later used to determine the fatigue life of the Ampelmann system. During telescoping motion of the gangway it was observed that the period of vibration decreases and increases when the T-boom is retracting and extending respectively. The fatigue life time analysis was done according to the stress life approach and rainflow cycle counting was used to obtain the number of stress cycles. The results show that the Ampelmann gangway can withstand up to 10^6 operational cycles. However, it should be emphasized that during operation external loadings are always present. Thus, the fatigue life time of the gangway will be lower than the expected number of operational cycles.

Contents

List of Figures

List of Symbols

Symbol	Description	Units
β	Torsional displacement; Newmark parameter	rad; –
γ	Newmark constant	–
δ	Log decrement parameter, nodal degrees of freedom	–
ϵ	Strain	–
ζ	Damping ratio	–
η	Strain rate damping parameter	s
θ	Slewing rotational angle	rad
κ	Curvature	m^{-2}
ρ	Steel density	$\frac{kg}{m^3}$
ρ_a	Air density	$\frac{kg}{m^3}$
φ	Luffing rotational angle	rad
Ω_b	Base excitation frequency	$\frac{rad}{s}$
ω_n	Natural frequency	$\frac{rad}{s}$
A	Cross sectional area	m^2
A_{eff}	Effective area	m^2
A_M	Main boom cross sectional area	m^2
A_{MT}	T-boomcross sectional area	m^2
A_T	Combined main and T-boom cross sectional area	m^2
a	Basquin parameter	–
B	Rate change in torsional displacement	$\frac{rad}{m}$
$B(t)$	Base excitation time function	m
b	Inverse slope of the S-N curve	–
C_D	Drag coefficient	–
c	Viscous damping	$\frac{N \cdot s}{m}$
c_{cr}	Critical damping	$\frac{Ns}{m}$
d	Shape function	–
E	Young's modulus	Pa
e	Distance from centroid to shear center	m
G	Shear modulus	Pa
I_g	Mass moment of inertia	$kg \cdot m^2$
I_{xx}	Second moment of inertia in x-axis	m^4
I_{zz}	Second moment of inertia in z-axis	m^4
J	Torsional constant	m^4
K	Stiffness matrix	$Pa \cdot m$
k	Negative inverse slope of the S-N curve; spring constant	–; $\frac{N}{m}$
k_r	Rotational spring stiffness	$\frac{N \cdot m}{rad}$
L_1	Length from base to the first connection	m
L_2	Length between the end of the main boom and the end of the T-boom	m
L_eff	Effective length	m
L_M	Main boom length	m

L_T	T-boom length	m
l_e	Element length	m
M	Moment	$N \cdot m$
m	Mass	kg
N	Fatigue life capacity	–
n_e	Number of elements	–
Q	Shear force	N
R_g	Radius of gyration	m
S_a	Stress amplitude	$\frac{N}{m^2}$
T	Torque	$N \cdot m$
t	Time variable	s
U_t	Telescoping velocity	$\frac{m}{s}$
V_w	Wind velocity	$\frac{m}{s}$
v	Horizontal deflection	m
w	Vertical deflection	m

1 Introduction

1.1. The Ampelmann system

The Ampelmann is an active motion compensation system, which stabilizes the transfer deck and gangway from the ship motion. The Ampelmann system is designed to enable safe and convenient transfer from ship to offshore structures by way of the gangway that is attached to the transfer deck. Figure 1.1 gives a representation of the Ampelmann system on board a vessel. The active motion compensation system measures

Figure 1.1: Ampelmann system.

the vessel motions continuously and stabilize the transfer. This is done by means of calculating the required length of the cylinders at each time step in order to keep the the transfer deck motionless. By compensating these motions, people can transfer safely from ship to a fixed offshore structure and vice-versa via a gangway. The Ampelmann system can be divided into two main systems. These system are the hexapod and the transfer deck with its gangway.

1.1.1. Hexapod

The Stewart platform of the Ampelmann system consist of a base frame, a top frame and the six hydraulic cylinders connected to the base and top frame, see Figure 1.2. The bottom frame is fixed to the vessel and the transfer deck rest on top of the top frame. The Stewart platform allows the transfer deck to move relative to the bottom frame.

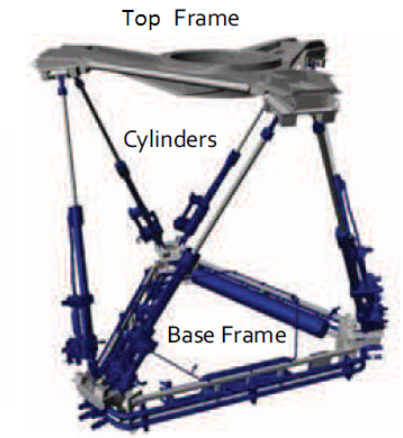

Figure 1.2: Stewart platform.

The control system of the Ampelmann is a Programmable Logic controller, which is responsible for the control of the Stewart platform. The Octans motion sensor measures the six degree of freedom motions of ship and sends the data to the Programmable Logic Controller. The Programmable Logic Controller used the measured data from the Octans to determine the required length of the cylinders during active motion compensation. The cylinder lengths are then sent back to the Programmable Logic Controller. A control loop that describes the control system in given in Figure 1.3.

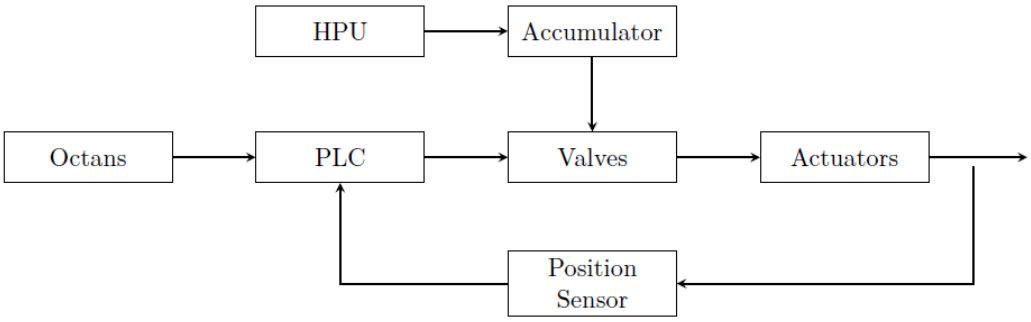

Figure 1.3: Control system loop.[16]

1.1.2. G25 gangway

Personnel accessing offshore structure from a ship from the Ampelmann system G25 Gangway structure consist of a Main Boom and a movable T-boom attached to the transfer deck. To position the gangway to an offshore structure during operation, the gangway is designed to be able to maneuver in three degrees of freedom, see Figure 1.4.

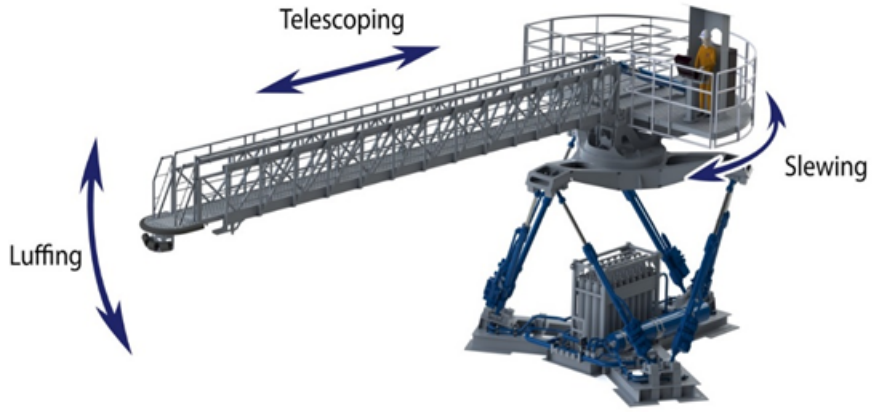

Figure 1.4: Gangway Degree of Freedom.

The three degrees of freedom movement of the gangway are:

- **Luffing**.
  Rotation around the horizontal x-axis, allowing the Gangway to ratate upwards or downwards.
- **Slewing**.
  Rotation around vertical z-axis, allowing the Gangway and transfer deck to rotate around its own base.
- **Telescoping**.
  Axial translation of the movable part of the gangway in the horizontal y-axis, allowing the movable part to be retracted or extended.

1.2. Research objective

Structural design of the Ampelmann Gangway is based on a set of static load cases which have been established in an early phase of the development of the product. Being in use for several years, regular reassessment of these load cases have been performed. Based on new applications of the stabilized gangways and the addition of various add-ons, new insights in the dynamics and study of structural phenomena such as fatigue became essential. One of the subjects which requires elaborate study is the occurrence of vibrations and shock loading in certain situations. Such dynamic loading may occur in different situations during operations. Examples are abrupt handling of the gangway controls, emergency retraction of the hexapod cylinders and vibrations resulting from the hydraulic control system.

The general objective in this thesis is directed towards in formulation of a dynamic model and to identify the fatigue life of the Ampelmann G25 gangway.

1.3. Thesis outline

The thesis outline in accordance to the thesis objective is given in total of six chapters. The first step in dynamic analysis is to investigate the background information needed to do the analysis and this is done in Chapter 2. In this chapter a review of the Euler-Bernoulli theory, damping in structure, numerical analysis and fatigue analysis is given. In Chapter 3 the Ampelmann G25 model is described in both horizontal and vertical direction. The results of the dynamic characteristics, response to external disturbance and response to gangway maneuvers are given in Chapter 4. In Chapter 5 one can find the fatigue life estimation of the

gangway using S-N approach. A comparison between different material damping parameter to the fatigue life is also shown. Chapter 6 summarizes the conclusion and recommendation of this research.

2

Theory

This chapter captures the theory behind the progress of this research. A brief discussion of Euler-Bernoulli beam model is given in Chapter 2.1. In Chapter 2.2 describes a few damping model in structural dynamics. Chapter 2.3 provides the principle of using numerical analysis. At last in Chapter 2.4 gives the theory behind fatigue analysis.

2.1. Euler-Bernoulli Beam Model

The Euler-Bernoulli beam theory cover cases for small deflection of beam subjected to lateral loads. The application restriction for applying the euler beam model are made up from the assumption that during deformation, plane sections remain plane and normal to the neutral axis.
Consider a free body diagram of an element of a slender beam displayed in figure 2.1, loaded with an external distributed force $f(x,t)$. The beam consist of a flexural stiffness EI, a cross sectional area A and a mass density ρ.

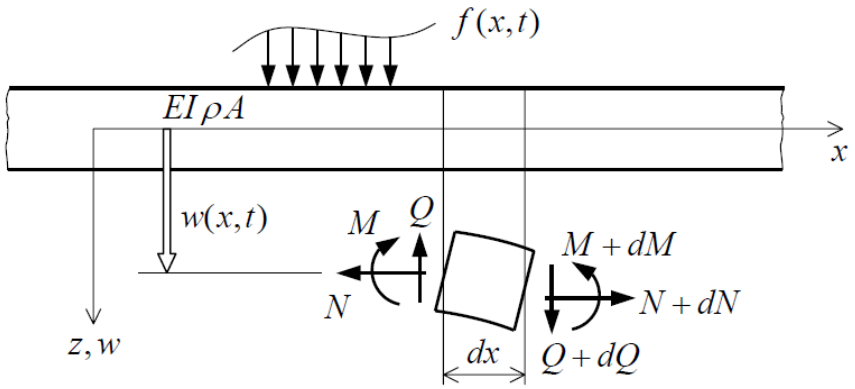

Figure 2.1: Beam Free body diagram.[12]

The symbol $w(x,t)$ in the figure denotes the displacement in positive z-direction. For small deflection the relation between strain ϵ, curvature κ and the slope ϕ of the deflection of the beam is as follows:

$$\begin{cases} \epsilon(z)) = z\kappa \\ \kappa = \frac{d\phi}{dx} \\ \phi = -\frac{dw(x)}{dx} \end{cases} \tag{2.1}$$

The bending moment $M(x)$ and the curvature are related by the stress, $\sigma(z) = E\epsilon(z)$, across its height of the beam. The expression of the bending moment is

$$M(x) = \int \sigma(z) z dA = -EI \frac{\partial^2 w}{\partial x^2} \tag{2.2}$$

By applying Newton's second law in the z-direction the equilibrium of forces is as follows:

$$dQ + f dx = \rho A dx \frac{\partial^2 w}{\partial t^2} \tag{2.3}$$

Note that Equation 2.4, the shear forces Q and $Q + dQ$ are considered to be directly vertical to each other, because the assumption of small deflections were made where the slopes are small and may be neglected. For small beam deflection the rotational inertia is generally neglected and balancing the moments gives the following relation for the shear force.

$$Q = \frac{\partial M}{\partial x} \tag{2.4}$$

From Equation 2.4 and 2.3 the partial differential equation that describes the transverse vibration of a beam in the neutral axis is expressed as

$$\rho A \frac{\partial^2 w(x,t)}{\partial t^2} + \frac{\partial^2}{\partial x^2}\left(EI \frac{\partial^2 w(x,t)}{\partial x^2}\right) = f(x,t) \tag{2.5}$$

2.2. Damping in structures

Damping can be described as the dissipation of energy from a system. The system energy, typically mechanical energy, is transformed or dissipated into other forms of energy. The damping, however is not necessarily a property of the system or structure itself, often the physical nature and its surrounding also causes the energy drainage. The damping sources in a structure can be described by damping, which occurs naturally within the structure, or due to its environment, or damping which is specially added to the system. According to [9] damping can be characterized as follows:

- **Fluid damping**.
  This type of damping is external to the structure and is related to the surrounding where the structure is. For example, damping effect due to soil-structure interaction at the foundation, flow-structure interaction.

- **Internal damping**.
  This type of damping is related to the material properties of the structure. The energy are dissipated through for example microscopic impurities, thermal elastic effects etcetera. The internal damping can be characterized into two general types: *viscoelastic damping* and *hysteretic damping*.
  The *viscoelastic damping* is a linear type damping depending on the frequency of vibration. In continuous systems it is addressed by the stress strain relation trough linear differential equation with respect to time. A common model representing the relationship, known as the Kelvin-Voigt model is given as

  $$\sigma = E\epsilon + \eta E \frac{d\epsilon}{dt}$$

  The *hysteretic damping* is a type of damping showing non linear characteristics. The damping does not significantly depends on the oscillating frequency as in the case of viscoelastic damping.

- **Structural damping**.
  This type of damping is related to the dissipation of the mechanical energy caused by friction from relative motion. For example, damping caused by the joints at the boundary of a structure.

Damping models are proposed in many literature. A suitable damping model should be chosen to represent the dissipation of energy in a structure.

2.2.1. Viscous damping

Viscous damping can be characterized as a linear damping. The damping force is linear proportional to the velocity and it is one of the most well known damping model in structural vibration. If the system vibrates with an instantaneous velocity $\dot{u}$, then viscous damping force is assumed to proportional to the instantaneous velocity, that is

$$F_d = c\dot{u} \tag{2.6}$$

where c is the damping coefficient and it determines the amount of damping within a system.
The viscous damping coefficient is mostly described along with the critical damping in terms of damping ratio between the two. The critical damping is the minimum amount of damping needed to prevent a system from oscillating and is related to the natural frequency of vibration. The damping ratio of a system is described with:

$$\zeta = \frac{c}{c_{cr}} = \frac{c}{2m\omega_n} \tag{2.7}$$

2.2.2. Aerodynamic damping

Wind loads occurs when the wind velocity increases or decreases near an obstacle. The relation between wind pressure and the velocity is derived from Bernoulli's law. This law states that the sum of kinetic energy of the airflow and the potential energy along a stream line is constant.
Energy can be dissipated by air in which a structure vibrates. Aerodynamic damping depends on both the velocity of incoming air and the velocity of the structure. According to[12] a mass spring system subjected to a wind, Figure 2.2, the equation of motion is as follows:

$$m\ddot{u} + c\dot{u} + ku = \frac{1}{2}\rho C_D A(v_w - \dot{u})^2 \tag{2.8}$$

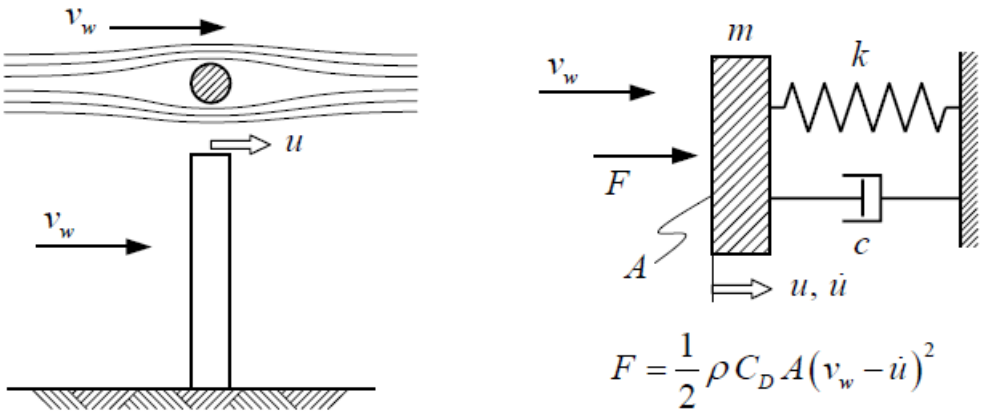

Figure 2.2: Structure exposing aerodynamic load.[12]

By assuming that the velocity of the vibrating structure is much lower than the velocity of the wind ($\dot{u} \ll v_w$), the equation of motion can be linearized to

$$m\ddot{u} + c\dot{u} + ku = \frac{1}{2}\rho C_D A(v_w^2 - 2v_w\dot{u}) \tag{2.9}$$

From Equation 2.9, one can see that there exist an extra positive damping related to the velocity of the wind given as

$$F_d = \rho C_D A v_w \dot{u}$$

2.2.3. Coulomb damping

Coulomb damping arises due to energy dissipation through dry friction. In other words, when a body slides on a dry surface creating friction forces resisting the sliding motion. On the point when the applied force to the system is larger that the friction force, the friction force is always opposite in the direction of the motion. The magnitude is independent of the surface area, displacement or velocity. According to [12] a single mass-spring system with coulomb damper can be schematically drawn as in Figure 2.3.

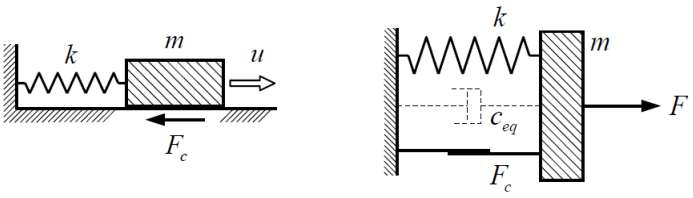

Figure 2.3: Coulomb damper.[12]

The equation of motion can be written in as

$$m\ddot{u} + F_c \frac{\dot{u}}{|\dot{u}|} + ku = 0$$

2.2.4. Damping measurement

Damping can be represented by various models and parameters. Estimating the realistic damping parameter is extremely difficult, mainly because it is not possible to eliminate the various types of damping (for example fluid damping, internal damping and structural damping). If one wishes to isolate one type of damping (e.g fluid damping), the actual measurement then would not represent the true damping model. Nevertheless, measuring the damping in a system, one should decide which model characterizes the most physical sense to the energy dissipation in a system. To measure the damping there are two general types to be distinguished, namely:

- **Time response method**.
  For example logarithmic decrement method, step response method and hysteric loop method.
- **Frequency response method**.
  For example magnification-factor method and bandwidth method.

One of the most common method to measure the damping is to use the time response logarithmic decrement method. Assessing the damping in a structure, the structure is set into free vibration by an initial impulse or an initial condition excitation. By recording and measuring the oscillating decay of the structure, the time response shown in Figure 2.4 takes the form as in Equation 2.10.

$$y(t) = y_0 e^{\zeta \omega_n t} \sin(\omega_d t) \tag{2.10}$$

where $\omega_d = \sqrt{1-\zeta^2}\omega_n$ is the damped natural frequency.

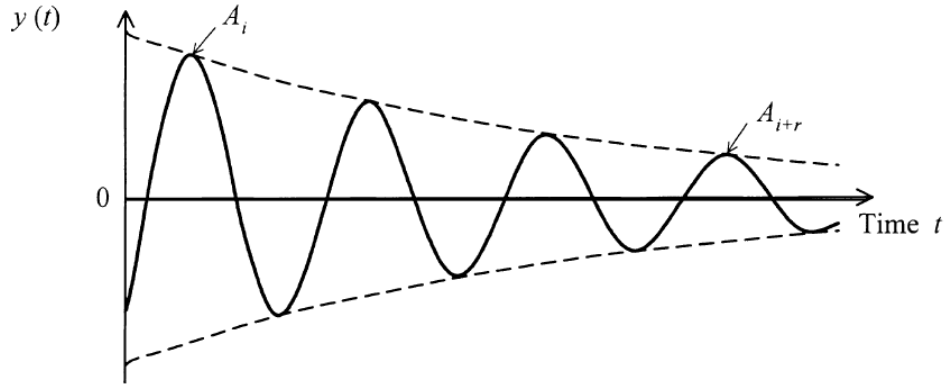

Figure 2.4: Vibration decay time response.[8]

If the response of a system is known, the logarithmic decrement δ can be obtained in order to identify the damping ratio of a structure. The log decrement can be defined as the natural log of the amplitudes of any two successive peaks and can be determined with

$$\delta = \frac{1}{r} \ln\left(\frac{A_i}{A_{i+r}}\right) \tag{2.11}$$

Where A_i amplitude of peak point of i cycle and A_{i+r} corresponds to the amplitude of the peak point of r cycles later in time.
The relation between the log decrement and the damping ratio is

$$\zeta = \frac{1}{\sqrt{1 + (\frac{2\pi}{\delta})^2}} \tag{2.12}$$

2.3. Numerical Analysis

Numerical analysis is the study of algorithms to approximate solutions to a complex mathematical problem. Most mathematical problems used in engineering are based on partial differential equation and ordinary differential equations where analytical solutions do not exist. In structural dynamics two types of numerical methods are primarily used to approximate the solution for these equations.
The first type is the *finite difference method* (FDM) which is the first and the oldest numerical approximation approach. The principle of finite difference method is to replace each derivative variable by a difference quotient by means of a local Taylor expansion near the point of interest.
The second type is the *finite element method* (FEM) and is the center of focus for solving partial differential equations in this study. The finite element method divides the structure into pieces of elements with their related physical quantities and approximates the solution in the equation by simpler function called shape functions. Conventionally the shape functions are chosen to be polynomials or piecewise polynomials[5].
In finite elements one can distinguish two types of boundary conditions, namely;

- **Essential boundary condition.**
  This type of boundary condition have to be appointed to the equation in order to solve for the solution. In beam analysis the field variables that describes the essential boundary conditions are the variables specifying either the displacement or rotation.

- **Natural boundary condition.**
  The natural boundary conditions are the higher order derivatives of the field variables. Hence, in beam analysis it is the variable related to the shear forces and moments. The shear forces and moments address themselves in the load vector and do not need to be appointed.

2.4. Uniaxial Fatigue analysis

Fatigue is defined as the the deterioration of a material under repeatedly cyclic loading. Fatigue properties of a material are obtained by testing a specimen at various load levels. The results of the test are plotted in terms of a log-log S-N curve.
An S-N curve gives a relation between stress amplitude, S_a and the cycles to failure, N. A schematic illustration of a typical S-N curve of a steel component usually on a log-log plot is given in Figure 2.5. The inclined regime is called the high cycle fatigue regime and the fatigue limit is given by the horizontal asymptote. The fatigue limit is defined as a fully reversed stress amplitude at which fatigue failure process begins with the occurrence of small cracks. If any applied stress to the structure falls below the fatigue limit of the material, the structure presumes to have an infinite life. This is one of the characteristics of structural aluminum alloys in calm environmental conditions.
Fatigue analysis using Stress-Life approach assumes all stresses at any point to be below the elastic limit. The mathematical relation expressing the S-N curve can be written as:

$$NS_a^k = a \tag{2.13}$$

Where a is the fatigue parameter which depends on the material property and is related to the intercept of the vertical axis.
The fatigue properties of a material is denoted by b or k in the high cycle regime. Both parameters are related in following expression:

$$k = -\frac{1}{b} \tag{2.14}$$

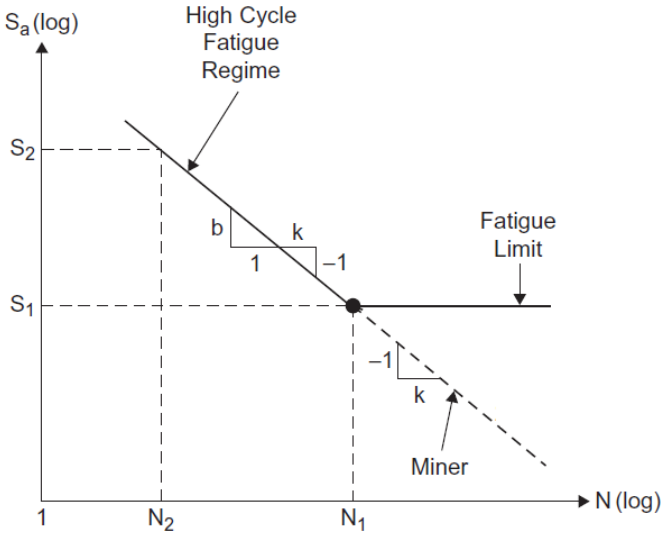

Figure 2.5: Constant amplitude S-N curve.

3

Ampelmann G25 gangway

3.1. Gangway beam Model

The Ampelmann G25 gangway consist of a Main Boom and a T-Boom attached to the transfer deck, see Figure 3.1a. The G25 gangway is connected to the transfer deck through hinges at the bottom and the top via two Luffing cylinders. This section concerns modeling the gangway using Euler-Bernoulli beam theory, also

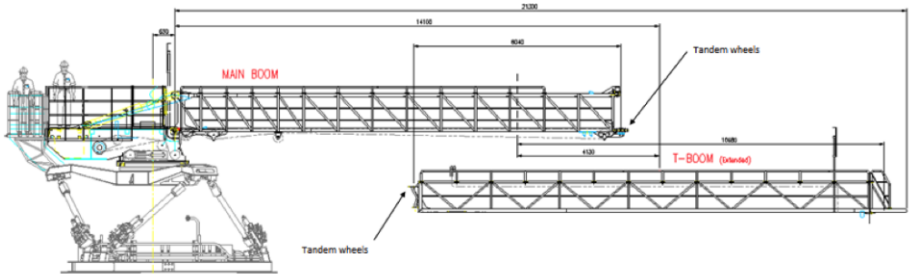

(a) Main and T-boom

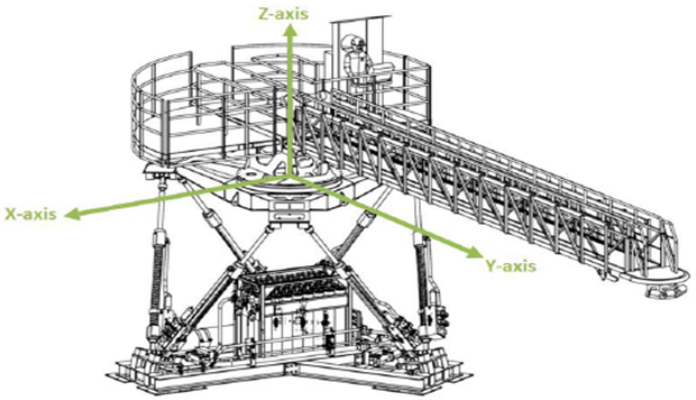

(b) Reference frame

Figure 3.1: Graphical overview of the gangway

known as the classical beam theory. As previously mentioned, the Euler-Bernoulli beam theory deal with cases for small deflection of beam subjected to lateral loads. The application restriction for applying the euler beam model are made up from the assumption that during deformation, plane sections remain plane and normal to the neutral axis. Using the reference frame Figure 3.1b, the gangway model is created by drawing

the boundary that the hexapod and the transfer deck are rigid, meaning that only analysis are to be made on the gangway with no structural influence of the hexapod and transfer deck, and by assuming that the T-boom is rigidly attached to the Main boom. Characterizing the gangway motion, a three step Euler beam model is used to describe the different part along the gangway and also material damping based on Kelvin-Voigt (or strain-rate) damping model is included to obtain the viscoelatic behavior of the gangway.

3.1.1. Gangway beam model z-y plane

The dynamic motion equation that describes the displacement of the gangway in z-axis facing the z-y plane, as shown in Figure 3.2, will be evaluated in this section.
As mentioned earlier, the gangway is supported by two luffing cylinders and hinges at the transfer deck. Due to the luffing cylinders, it is expected that rotational stiffness k_r is present at the connection. Since the dead weight only influence the static deflection of the gangway, it is assumed that it does not influence the dynamics of the system. A graphical representation can be seen in Figure 3.2 and the set of equations of motions

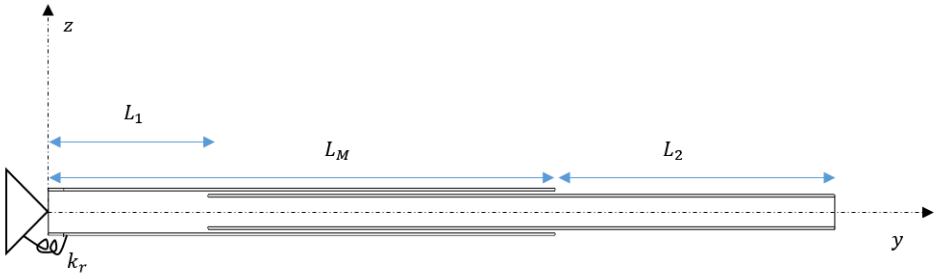

Figure 3.2: Beam model in the z-y plane

that describe the vibration, valid for any point on the gangway except at the boundary and interfaces, in this axis can be written as:

$$\begin{cases} \rho A_M \frac{\partial^2 w_1}{\partial t^2} + (EI_{zz})_M \frac{\partial^4 w_1}{\partial y^4} + \left(\eta EI_{zz}\right)_M \frac{\partial^5 w_1}{\partial y^4 \partial t} = 0, & 0 \le y \le L_1(y) \\ \rho (A_M + A_T) \frac{\partial^2 w_2}{\partial t^2} + (EI_{zz})_{MT} \frac{\partial^4 w_2}{\partial y^4} + \left(\eta EI_{zz}\right)_{MT} \frac{\partial^5 w_2}{\partial y^4 \partial t} = 0, & L_1(y) \le y \le L_M \\ \rho A_T \frac{\partial^2 w_3}{\partial t^2} + (EI_{zz})_T \frac{\partial^4 w_3}{\partial y^4} + \left(\eta EI_{zz}\right)_T \frac{\partial^5 w_3}{\partial y^4 \partial t} = 0, & L_M \le y \le L_2(y) \end{cases} \tag{3.1}$$

The associated boundary condition required contains properties in terms of kinematic and dynamic balance at both ends. Boundary condition from kinematic demands are from the equilibrium in both displacement and rotation, while dynamic demands are from the equilibrium in forces and moments. The equilibrium condition at both boundaries read:

at $y = 0$

$$w_1 = 0 \qquad \text{and} \qquad \left(E + \eta E \frac{\partial}{\partial t}\right)(I_{zz})_M \frac{\partial^2 w_1}{\partial y^2} = k_r \frac{\partial w_1}{\partial y} \tag{3.2}$$

at $y = L$

$$\left(E + \eta E \frac{\partial}{\partial t}\right)(I_{zz})_T \frac{\partial^2 w_3}{\partial y^2} = 0 \qquad \text{and} \qquad \left(E + \eta E \frac{\partial}{\partial t}\right)(I_{zz})_T \frac{\partial^3 w_3}{\partial y^3} = 0 \tag{3.3}$$

To complete the mathematical expression, the interface condition to allow for the continuity and balance of forces of the different cross section and stiffness of the first connection at L_1 and the second connection at L_m also follow from the kinematic and dynamic equilibrium.

at $y = L_1$

$$w_1 = w_2$$

$$\frac{\partial w_1}{\partial y} = \frac{\partial w_2}{\partial y}$$

$$\left(E + \eta E \frac{\partial}{\partial t}\right)(I_{zz})_M \frac{\partial^2 w_1}{\partial y^2} = \left(E + \eta E \frac{\partial}{\partial t}\right)(I_{zz})_{MT} \frac{\partial^2 w_2}{\partial y^2} \tag{3.4}$$

$$\left(E + \eta E \frac{\partial}{\partial t}\right)(I_{zz})_M \frac{\partial^3 w_1}{\partial y^2} = \left(E + \eta E \frac{\partial}{\partial t}\right)(I_{zz})_{MT} \frac{\partial^3 w_2}{\partial y^2}$$

at $y = L_M$

$$w_2 = w_3$$

$$\frac{\partial w_2}{\partial y} = \frac{\partial w_3}{\partial y}$$

$$\left(E + \eta E \frac{\partial}{\partial t}\right)(I_{zz})_{MT} \frac{\partial^2 w_2}{\partial y^2} = \left(E + \eta E \frac{\partial}{\partial t}\right)(I_{zz})_T \frac{\partial^2 w_3}{\partial y^2} \tag{3.5}$$

$$\left(E + \eta E \frac{\partial}{\partial t}\right)(I_{zz})_{MT} \frac{\partial^3 w_2}{\partial y^2} = \left(E + \eta E \frac{\partial}{\partial t}\right)(I_{zz})_T \frac{\partial^3 w_3}{\partial y^2}$$

The above mentioned $w_1..w_3$ is the displacement in the z-direction, η is the strain rate damping parameter, ρ is the density of the gangway, E is the Young's modulus and $A_{M,MT,T}$ and $Izz_{M,MT,T}$ is the area and second moment of inertia corresponding to the main boom, the overlapping section and the T-boom.

3.1.2. Gangway beam model in x-y plane

The dynamic motion equation that describes the displacement of the gangway in x-axis facing the x-y plane is discussed.
Given that the shape of the gangway is a U-shape like beam, as can be seen in Figure 3.3b, means that the gangway is having only one cross-section symmetry in the z-axis. Vibration in the x-axis will cause a coupled

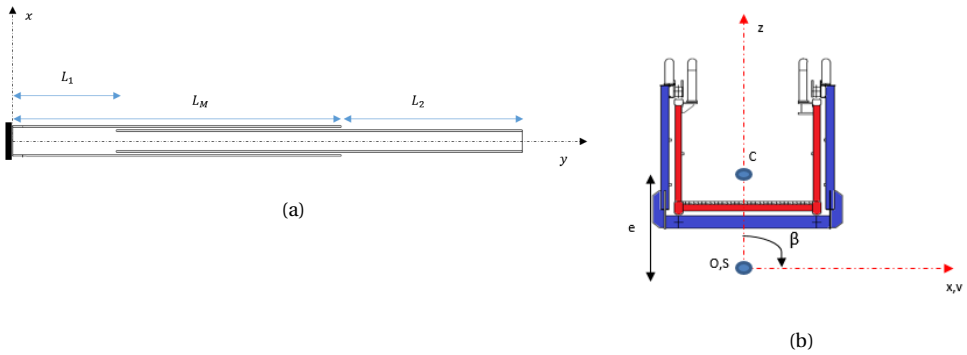

Figure 3.3: Beam model in the z-y plane.

bending-torsional displacement, because the shear center (s) and the centroid (c) of the beam cross-section does not coincide.

Torsional behavior of an open cross section deal with out of plane deformation is called warping. However, during analysis it is assumed that the torsional rotation is a linear function along the gangway axis and the out of plane deformation are small relative to the dimension of the cross section. This implies that torsional rotation at both ends are equal so that warping can be neglected. According to [17], the bending-torsional equation of motion can be recorded by coupling the Euler-Bernoulli and Saint-Venant beam theory. The set of differential equations of motions for coupled bending and torsional vibrations of a three stepped gangway model can be written as

Bending motion

$$\begin{cases} \rho A_M \frac{\partial^2 v_1}{\partial t^2} + (EI_{xx})_M \frac{\partial^4 v_1}{\partial y^4} + \left(\eta EI_{xx}\right)_M \frac{\partial^5 v_1}{\partial y^4 \partial t} + \rho A_M e \frac{\partial^2 \beta_1}{\partial t^2} = 0, & 0 \le y \le L_1(y) \\ \rho (A_M + A_T) \frac{\partial^2 v_2}{\partial t^2} + (EI_{xx})_{MT} \frac{\partial^4 v_2}{\partial y^4} + \left(\eta EI_{xx}\right)_{MT} \frac{\partial^5 v_2}{\partial y^4 \partial t} + \rho (A_M + A_T) e \frac{\partial^2 \beta_2}{\partial t^2} = 0, & L_1(y) \le y \le L_M \\ \rho A_T \frac{\partial^2 v_3}{\partial t^2} + (EI_{xx})_T \frac{\partial^4 v_3}{\partial y^4} + \left(\eta EI_{xx}\right)_T \frac{\partial^5 v_3}{\partial y^4 \partial t} + \rho A_M e \frac{\partial^2 \beta_3}{\partial t^2} = 0, & L_M \le y \le L_2(y) \end{cases} \tag{3.6}$$

Torional motion

$$\begin{cases} \left(I_{g_s}\right)_M \frac{\partial^2 \beta_1}{\partial t^2} - (GJ)_M \frac{\partial^2 \beta_1}{\partial y^2} - \left(\eta GJ\right)_M \frac{\partial^3 \beta_1}{\partial y^2 \partial t} + \rho A_M e \frac{\partial^2 v_1}{\partial t^2} = 0, & 0 \le y \le L_1(y) \\ \left(I_{g_s}\right)_{MT} \frac{\partial^2 \beta_2}{\partial t^2} - (GJ)_{MT} \frac{\partial^2 \beta_2}{\partial y^2} - \left(\eta GJ\right)_{MT} \frac{\partial^3 \beta_2}{\partial y^2 \partial t} + \rho A_{MT} e \frac{\partial^2 v_2}{\partial t^2} = 0, & L_1(y) \le y \le L_M \\ \left(I_{g_s}\right)_T \frac{\partial^2 \beta_3}{\partial t^2} - (GJ)_T \frac{\partial^2 \beta_3}{\partial y^2} - \left(\eta GJ\right)_T \frac{\partial^3 \beta_3}{\partial y^2 \partial t} + \rho A_T e \frac{\partial^2 v_3}{\partial t^2} = 0, & L_M \le y \le L_2(y) \end{cases} \tag{3.7}$$

The connection between the main boom and the transfer deck is supported by assuming a clamped connection. The effect of the luffing cylinder is left out, because the luffing cylinders can only move in the vertical degree of freedom.
Again applying the kinematic and dynamic balance for both bending and torsion, the boundary conditions are as follows:

at $y = 0$

$$v_1 = 0 \quad \text{and} \quad \frac{\partial v_1}{\partial y} = 0 \quad \text{and} \quad \beta_1 = 0 \tag{3.8}$$

at $y = L$

$$\left(E + \eta E \frac{\partial}{\partial t}\right)(I_{xx})_T \frac{\partial^2 v_3}{\partial y^2} = 0 \quad \text{and} \quad \left(E + \eta E \frac{\partial}{\partial t}\right)(I_{xx})_T \frac{\partial^3 v_3}{\partial y^3} = 0 \quad \text{and} \quad \left(G + \eta G \frac{\partial}{\partial t}\right) J_T \frac{\partial \beta_3}{\partial y} = 0 \tag{3.9}$$

The corresponding interface condition at the first connection(L_1) and the second connection(Lm) for continuity and balance of forces reads:

at $y = L_1$

$$
\begin{gathered}
v_1 = v_2 \\
\frac{\partial v_1}{\partial y} = \frac{\partial v_2}{\partial y} \\
\left(E + \eta E \frac{\partial}{\partial t}\right)(I_{xx})_M \frac{\partial^2 v_1}{\partial y^2} = \left(E + \eta E \frac{\partial}{\partial t}\right)(I_{xx})_{MT} \frac{\partial^2 v_2}{\partial y^2} \\
\left(E + \eta E \frac{\partial}{\partial t}\right)(I_{xx})_M \frac{\partial^3 v_1}{\partial y^2} = \left(E + \eta E \frac{\partial}{\partial t}\right)(I_{xx})_{MT} \frac{\partial^3 v_2}{\partial y^2} \\
\beta_1 = \beta_2 \\
\left(G + \eta G \frac{\partial}{\partial t}\right) J_M \frac{\partial \beta_1}{\partial y} = \left(G + \eta G \frac{\partial}{\partial t}\right) J_{MT} \frac{\partial \beta_2}{\partial y}
\end{gathered}
\tag{3.10}
$$

at $y = L_M$

$$
\begin{gathered}
v_2 = v_3 \\
\frac{\partial v_2}{\partial y} = \frac{\partial v_3}{\partial y} \\
\left(E + \eta E \frac{\partial}{\partial t}\right)(I_{xx})_{MT} \frac{\partial^2 v_2}{\partial y^2} = \left(E + \eta E \frac{\partial}{\partial t}\right)(I_{xx})_T \frac{\partial^2 v_3}{\partial y^2} \\
\left(E + \eta E \frac{\partial}{\partial t}\right)(I_{xx})_{MT} \frac{\partial^3 v_2}{\partial y^2} = \left(E + \eta E \frac{\partial}{\partial t}\right)(I_{xx})_T \frac{\partial^3 v_3}{\partial y^2} \\
\beta_2 = \beta_3 \\
\left(G + \eta G \frac{\partial}{\partial t}\right) J_{MT} \frac{\partial \beta_2}{\partial y} = \left(G + \eta G \frac{\partial}{\partial t}\right) J_T \frac{\partial \beta_3}{\partial y}
\end{gathered}
\tag{3.11}
$$

3.2. Gangway cross section parameters

Calculating the cross sectional parameters of the gangway is not a straight forward task. The gangway is a truss like profile and may affect the validity of theories to be applied. In this section the gangway parameters needed to analyze the dynamic characteristic are explained.

3.2.1. Second moment of area

Second moment of inertia of truss structure like the Main and T-boom is difficult to calculate. One can use a numerical program to obtain the relevant values. However, it is assumed that the four main bars are the most contributing structural component to the second moment of inertia. A simplified drawing of the four main bars is given in Figure 3.4

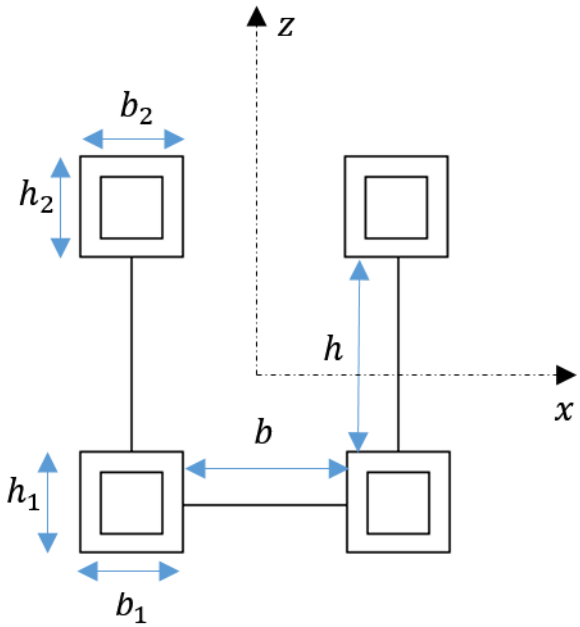

Figure 3.4: Cross sectional members of a beam.

Using the bar as reference, the second moment of inertia can be formulated by using the parallel axis theorem and the expression for its relevant axis is expressed as follow:

$$\begin{cases} I_{zz} = \sum \left(I_{z_i} + A_i \left(z_{cog} - z_{cog_i} \right)^2 \right) \\ I_{xx} = \sum \left(I_{x_i} + A_i \left(x_{cog} - x_{cog_i} \right)^2 \right) \end{cases} \tag{3.12}$$

Where A_i, z_{cog_i}, x_{cog_i} denotes the corresponding area and center of gravity values of each of the members and z_{cog} and x_{cog} are the center of gravity of the total system.

3.2.2. Shear center

Shear center is an imaginary point on or outside the section through which an external load is applied without inducing any twisting of the structure. For a complex cross section like the gangway, the shear center is not easily computed.
In this work the shear center of the Main and T-boom are determined using the numerical program Ansys workbench. The structural component of the gangway are drawn and modeled as line beam element in Ansys. By varying the point where the remote force is applied, the location of the shear center of both the Main and T-boom can be obtained.

3.2.3. Torsional rigidity

The torsional rigidity J for well known geometries are available, whereas for cross sections like Main boom and T-boom requires numerical program to obtain the torsional rigidity.
To obtain the torsional rigidity of the Main and T-boom, the model drawn in the numerical program Ansys Workbench is used. With the shear center already determined in the previous section, the angle of twist β with respect to the shear center can be obtained by applying a remote torque to the beam and measured its

vertical and horizontal displacement. Knowing both the angle of twist and the applied torque, the torsion rigidity GJ can be obtained using the relation

$$T = \frac{GJ\beta}{L} \tag{3.13}$$

where L is the length of the beam.

3.2.4. Mass moment of inertia

As said earlier, the Ampelmann gangway is made of frame structure and their properties can not be easily determined. The mass moment of inertia of the Main and the T-Boom around the shear center is obtained by first estimating the radius of gyration in Autocad. The relation between the radius of gyration and the mass moment of inertia is given as

$$R_{g_{axis}} = \frac{I_{g_{axis}}}{m} \tag{3.14}$$

Where $R_{g_{axis}}$ is the radius of gyration, $I_{g_{axis}}$ is the mass moment of inertia corresponding to its relevant axis and m denotes the mass of the system.

3.2.5. Damping

The damping characteristic of the G25 gangway in vertical (z-axis) direction are determined by a free vibration test. The test was conducted by applying a mass of $300kg$ at the tip of the fully extended gangway. The mass was then released from the gangway causing the gangway to vibrate. The measured displacement as a function of time is given Figure 3.6.

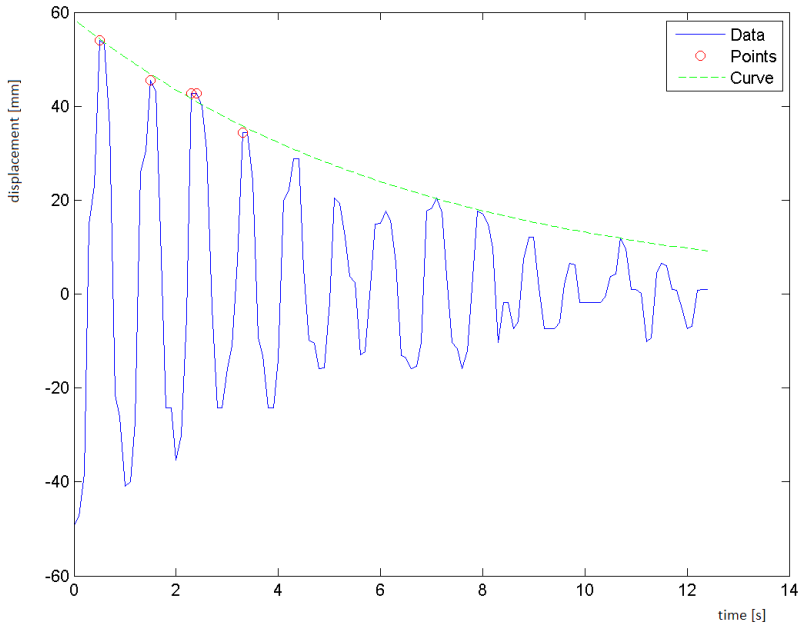

Figure 3.5: Free vibration test curve

Using the log decrement method, the damping ratio of the gangway can be obtained. From the experimental graph, one can see that the first peak at $t \approx 0.5s$ the amplitude $y(t \approx 0.5) = 57$. Another peak at different time

instance at $t \approx 3s$, the peak value is $y(t \approx 2) = 41)$. The number of cycles $r = 2$ and gives a decrement value of

$$\delta = \frac{1}{r} \ln\left(\frac{A_i}{A_{i+r}}\right) = 0.165$$

The non dimensional damping coefficient of the system is

$$\zeta = \frac{1}{\sqrt{1 + (\frac{2\pi}{\delta})^2}} = 0.026$$

Knowing the damping ratio, the kelvin-Voight damping parameter η of a continuous can be obtained using

$$\eta = \frac{2}{\omega_n} \zeta = 0.0089s \tag{3.15}$$

An analysis of the tip deflection using the obtained damping parameter as input is with the same initial condition as the measured data shown in the figure below.

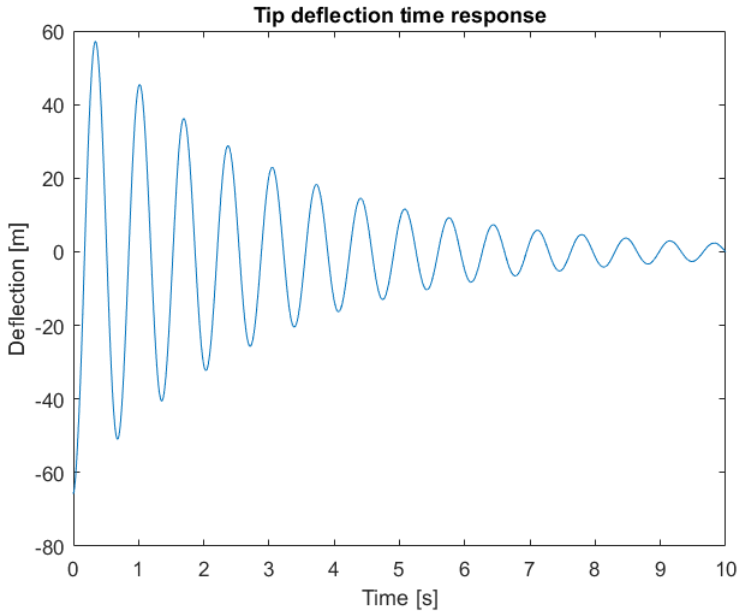

Figure 3.6: Modeled tip deflection response with $\eta = 0.0089s$.

Influence of the material damping

As can be observed, adding material damping to the system gave an exponentially decay to the vibration response. The calculated damping ratio along with its material damping value is an approximation to the experimental system response. A study for different material damping η values, see Figure 3.7, was performed to compare the sensitivity of the gangway to the approximate value.
From the figure one can see that if the material damping have a great effect on the response of the system. It can be seen that with the presence of material damping, higher modes damped out faster than lower modes.

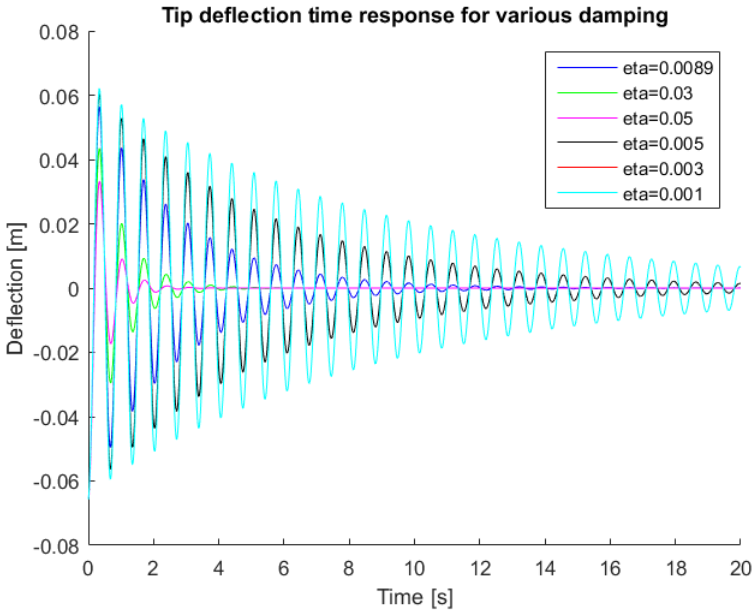

Figure 3.7: Influence of different material damping for free vibration

4

Dynamic Analysis

The Ampelmann gangway beam models introduced in Chapter 3.1 were used to analyze the dynamics and characteristics. In this chapter the free vibration defined by its characteristics natural frequency and mode shapes and vibration under external applied loading are reviewed. Solving the partial differential equation of motion analytically with arbitrary boundary condition is difficult to obtain. It involves solving at least a 12 by 12 determinant. Although, solving large determinant is still possible, it is more efficient to employ numerical approximation. A linear one dimensional Finite Element Analysis was performed and implemented in MATLAB to solve for the system equation of motion.

4.1. Finite element formulation

One of the most versatile method to solve engineering problem is by using Finite Element Method (FEM), which divide the structure into number of elements (N) with their related physical quantities. The finite element discretization of one-dimensional problems are characterized by a two point boundary problem.

Bending motion

To illustrate this procedure, consider a beam element of length le, flexural rigidity $EI(y)$ and mass per unit length $\rho A(x)$ shown in Figure 4.1. The two points mutually joined or interconnected to each other are called nodes. In finite element modeling the transverse vibration of a beam where planar displacement are governed by a fourth order differential equation, depends on the knowledge of four boundary condition at an inter-element. Every beam element requires a continuous nodal transverse displacement w and slope θ.

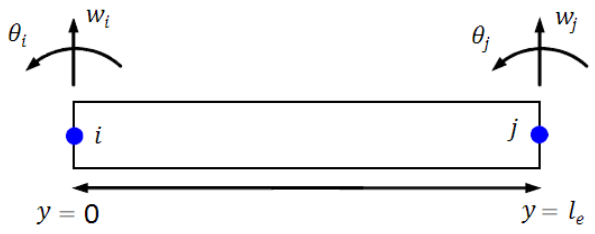

Figure 4.1: Two node beam element.

Between the two nodes, the continuity of the bending displacement and slope of a beam element can be satisfied by using Hermite polynomials function. To derive the shape functions the minimum possible poly-

nomial in order to fulfil both the compatibility and continuity is of cubic form and is given as [5]

$$w(y) = c_0 + c_1 y + c_2 y^2 + c_3 y^3 \tag{4.1}$$

Where, $c_0..c_3$ are the coefficients of the cubic polynomial determined from the inter-element boundary condition by employing the following conditions.

$$\begin{aligned} w(0) &= w_i \\ \left.\frac{dw}{dy}\right|_{y=0} &= \theta_i \\ w(l_e) &= w_j \\ \left.\frac{dw}{dy}\right|_{y=l_e} &= \theta_j \end{aligned} \tag{4.2}$$

Evaluating the coefficients c_j in terms of the nodal displacement and rotation, one can obtain the solution in the form

$$w(y) = \begin{bmatrix} d_1(y) & d_2(y) & d_2(y) & d_4(y) \end{bmatrix} \begin{bmatrix} w_i \\ \theta_i \\ w_j \\ \theta_j \end{bmatrix} \tag{4.3}$$

The Hermite shape functions d_i which gives an approximated interpolation for the transverse displacement and rotation of the beam is given as

$$\begin{aligned} d_1(y) &= 1 - \tfrac{3y^2}{l_e^2} + \tfrac{2y^3}{l_e^3} \\ d_2(y) &= y - \tfrac{2y^2}{l_e} + \tfrac{y^3}{l_e^2} \\ d_3(y) &= \tfrac{3y^2}{l_e^2} - \tfrac{2y^3}{l_e^3} \\ d_3(y) &= -\tfrac{y^2}{l_e} + \tfrac{y^3}{l_e^2} \end{aligned} \tag{4.4}$$

With the shape functions, one can develop the mass and stiffness matrix of the beam element. The kinetic energy and the strain energy of a bending Euler-Bernoulli beam is given as follows:

$$E_{kin} = \frac{1}{2}\int_0^{l_e} \rho A(y) \left(\tfrac{\partial w}{\partial t}\right)^2 dy \tag{4.5}$$

$$E_{pot} = \frac{1}{2}\int_0^{l_e} EI(y) \left(\tfrac{\partial^2 w}{\partial y^2}\right)^2 dy \tag{4.6}$$

Upon substituting equation 4.3 into 4.5 and 4.6 and solving for the integral, the mass and stiffness matrix of a bending beam is found as

$$[M_{EI}] = \frac{\rho A l_e}{420} \begin{bmatrix} 156 & 22l_e & 54 & -13l_e \\ 22l_e & 4l_e^2 & 13l_e & -3l_e^2 \\ 54 & 13l_e & 156 & -22l_e \\ -13l_e & -3l_e^2 & -22l_e & 4l_e^2 \end{bmatrix} \tag{4.7}$$

$$[K_{EI}] = \frac{EI}{l_e^3} \begin{bmatrix} 12 & 6l_e & -12 & 6l_e \\ 6l_e & 4l_e^2 & -6l_e & 2l_e^2 \\ -12 & -6l_e & 12 & -6l_e \\ 6l_e & 2l_e^2 & -6l_e & 4l_e^2 \end{bmatrix} \tag{4.8}$$

Coupled bending torsional motion

A beam experiencing coupled bending and torsional vibrations the kinetic energy and strain energy to the

equation of motion in Chapter 3.1.2 can be written as

$$E_{kin} = \frac{1}{2}\int_0^{l_e}\left(\rho A(y)\left[\frac{\partial v}{\partial t}\right]^2 + \rho A(y)e\left[\frac{\partial v}{\partial t}\frac{\partial \beta}{\partial t}\right] + I_g(y)\left[\frac{\partial \beta}{\partial t}\right]^2\right)dy \tag{4.9}$$

$$E_{pot} = \frac{1}{2}\int_0^{l_e}\left(EI(y)\left[\frac{\partial^2 v}{\partial y^2}\right]^2 + GJ(y)\left[\frac{\partial \beta}{\partial y}\right]\right)dy \tag{4.10}$$

Consider a beam element with the nodes defined on the shear center as shown in 4.2. Each node is having four degrees of free from namely the bending displacement v, bending slope (θ), torsional rotation (β) and torsional slope(B). Again using cubic polynomials as shape function for the flexural displacement and

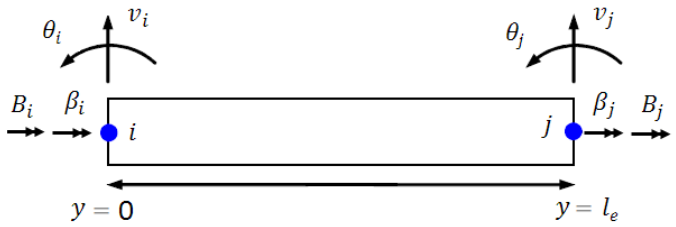

Figure 4.2: Two node beam element with 8 degrees of freedom

torsional rotation, the nodal displacements of the coupled motion takes the form

$$\begin{bmatrix} v \\ \beta \end{bmatrix} = \begin{bmatrix} d_1(y) & d_2(y) & d_2(y) & d_4(y) \end{bmatrix} \begin{bmatrix} v_i & \beta_i \\ \theta_i & B_i \\ w_j & \beta_j \\ \theta_j & B_j \end{bmatrix} \tag{4.11}$$

By substituting Equation 4.11 in the strain and kinetic energy relation and performing the integration, the 8×8 stiffness and consistent mass matrix can be written in the following form

$$K_c = \begin{bmatrix} K_{EI} & 0 \\ 0 & K_{GJ} \end{bmatrix} \tag{4.12}$$

$$M_c = \begin{bmatrix} M_{EI} & eM_{EI} \\ eM_{EI}^T & M_{GJ} \end{bmatrix} \tag{4.13}$$

The corresponding sub matrices K_{GJ}, M_{GJ} are given as

$$K_{GJ} = GJ \begin{bmatrix} \frac{6}{5l_e} & \frac{1}{10} & -\frac{6}{5l_e} & \frac{1}{10} \\ \frac{1}{10} & \frac{2l_e}{15} & -\frac{1}{10} & -\frac{1}{30} \\ -\frac{6}{5l_e} & -\frac{1}{10} & \frac{6}{5l_e} & -\frac{1}{10} \\ \frac{1}{10} & -\frac{1}{30} & -\frac{1}{10} & \frac{2l_e}{15} \end{bmatrix} \tag{4.14}$$

$$M_{GJ} = \frac{I_g l_e}{420} \begin{bmatrix} 156 & 22l_e & 54 & -13l_e \\ 22l_e & 4l_e^2 & 13l_e & -3l_e^2 \\ 54 & 13l_e & 156 & -22l_e \\ -13l_e & -3l_e^2 & -22l_e & 4l_e^2 \end{bmatrix} \tag{4.15}$$

Approximating the fourth order partial differential equation of the beam with finite elements, the set of equation of motion reduces to a system of ordinary differential equation in the form

$$[\boldsymbol{M}]\ddot{\delta} + [\boldsymbol{C}]\dot{\delta} + [\boldsymbol{K}]\delta = \boldsymbol{F(t)} \tag{4.16}$$

Where $\boldsymbol{M}$, $\boldsymbol{C}$ and $\boldsymbol{K}$ denotes the global mass, damping and stiffness matrix. The symbols δ and F are the displacement and forcing vector.
The material damping added to the system is proportional to the stiffness the of the gangway. Therefore, rewriting the ordinary differential equation gives

$$[\boldsymbol{M}]\ddot{\delta} + \eta[\boldsymbol{K}]\dot{\delta} + [\boldsymbol{K}]\delta = \boldsymbol{F(t)} \tag{4.17}$$

4.2. Free vibration analysis

Finding the natural frequencies and modes shape concerns for solving the system equation of motion without damping and external applied force. For an ordinary differential equation the characteristic dynamic behavior of the gangway can be found by solving the equation

$$\left([\boldsymbol{K}]\ddot{\delta} - \omega_n^2[\boldsymbol{M}]\right)\delta = 0 \tag{4.18}$$

where the eigenvalue ω_n^2 represents the natural frequency and the eigenvector δ represents the mode shape or the displacement profile of the system.

4.2.1. Natural frequencies and mode shapes z-y plane

Based on the parameters and material properties of the G25 gangway given in Appendix A, the dynamic characteristics can be analyzed. The results of the first five natural frequencies and mode shapes of the Ampelmann gangway in fully extended configuration are shown in Table 4.1 and in Figure 4.3, respectively:

Table 4.1: Vertical z-y plane natural frequencies of a fully extended gangway

Mode number	$1st$	$2nd$	$3rd$	$4th$	$5th$
Natural frequency $[\frac{rad}{s}]$	6.03	34.81	107.88	208.60	367.25
Natural frequency $[Hz]$	0.96	5.54	17.17	33.2	58.45

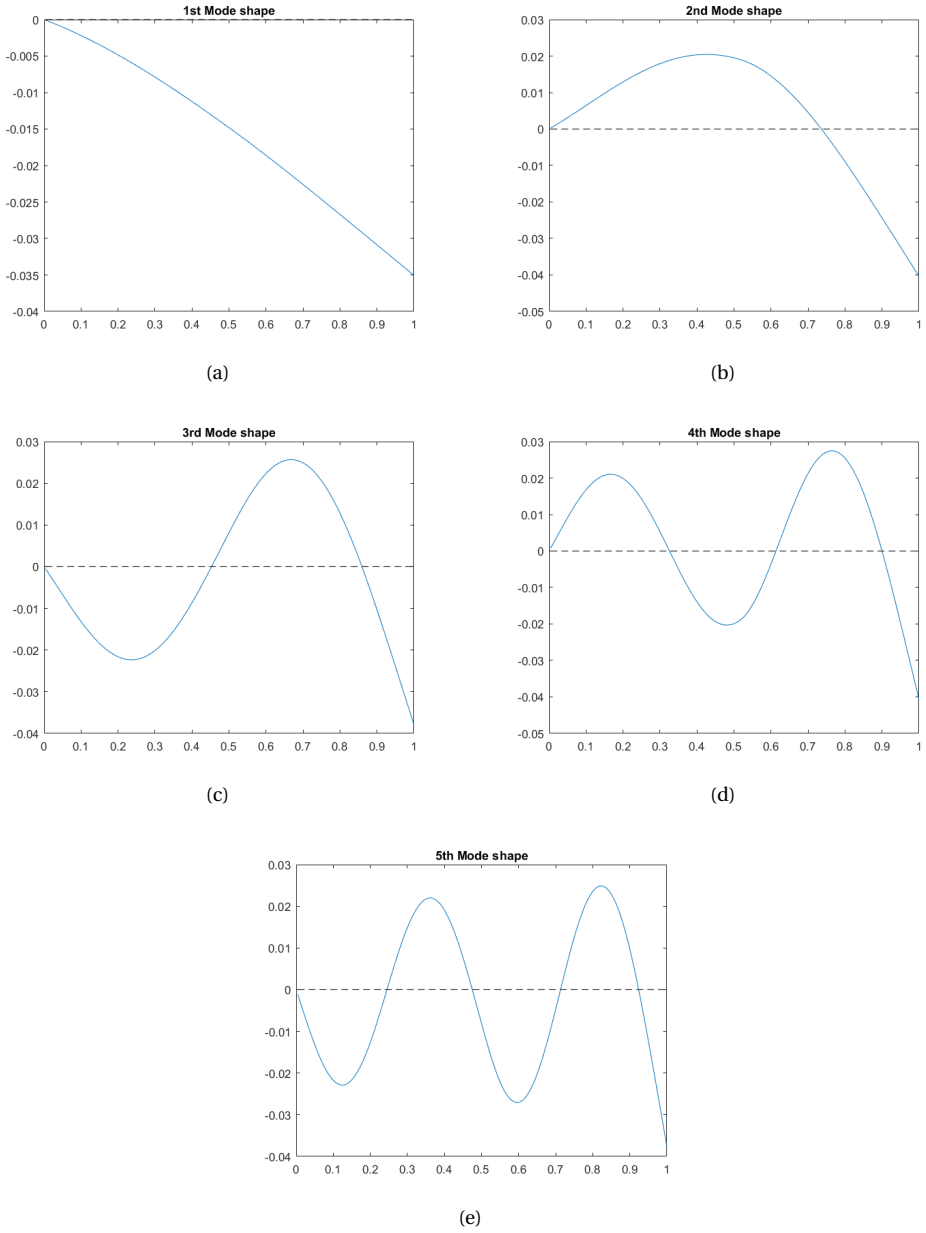

(a) (b) (c) (d) (e)

Figure 4.3: Graphical overview of the first five mode shapes.

4.2.2. Natural frequencies and mode shapes x-y plane Natural frequencies and mode shapes

As discussed in Chapter 3.1.2, vibration in this plane is coupled with a bending torsional motion due to the offset of the shear center. The full extended gangway natural frequencies and its mode shape are shown in Table 4.2 and Figure 4.4.

Table 4.2: Horizontal z-y plane natural frequencies of a fully extended gangway

Mode number	$1st$	$2nd$	$3rd$	$4th$	$5th$
Natural frequency $[\frac{rad}{s}]$	2.84	8.05	10.29	13.74	18.98
Natural frequency $[Hz]$	0.45	1.28	1.64	2.19	3.02

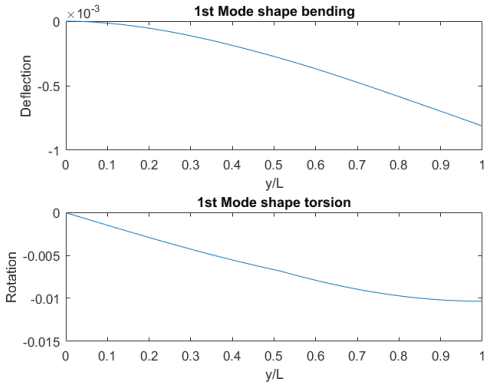

(a)

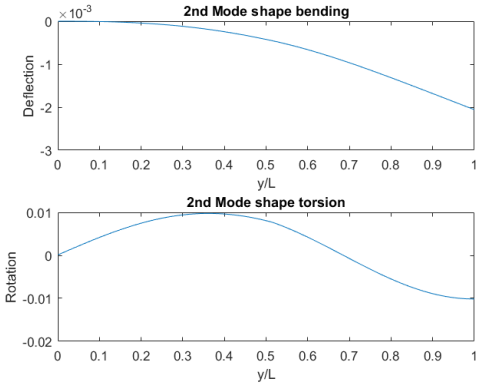

(b)

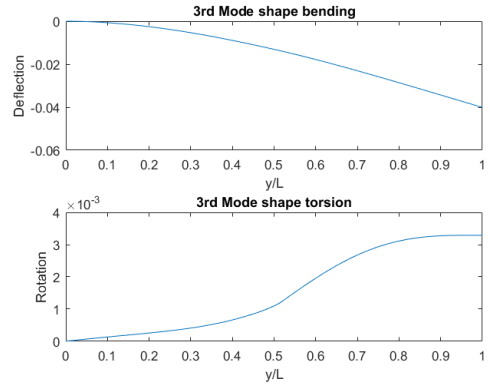

(c)

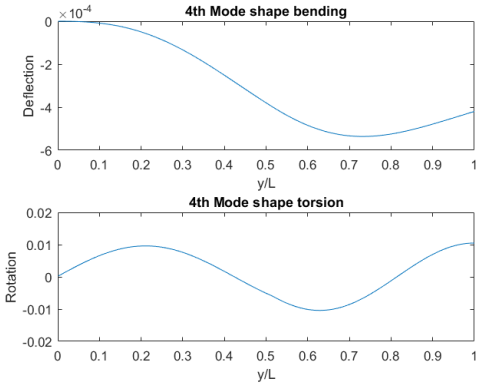

(d)

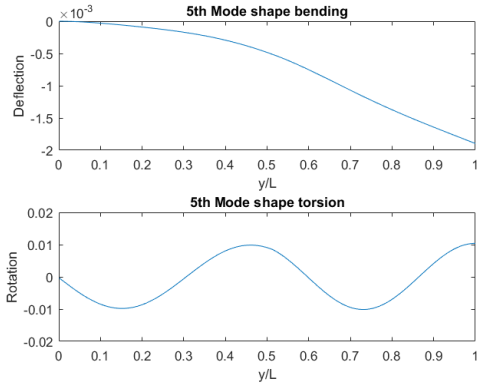

(e)

Figure 4.4: Graphical overview of the first five Coupled mode shapes.

4.3. Dynamic response to external disturbance

This section will investigate the vibration of the gangway under base excitation and constant wind. First, the gangway under base excitation is assessed, after which the analysis under constant wind velocity is explained.

4.3.1. Vibration under base excitation

In this analysis the vibration is caused hexapod induced motion on the transfer deck or in this case the base of the gangway. Mathematical modeling the ship induced motion to the hexapod is beyond the scope of this thesis. A straight forward way to obtain the motion at the base is by taking measurements on the transfer deck of the Ampelmann system.
Consider the gangway subjected to a base excitation as shown in Figure 4.5.

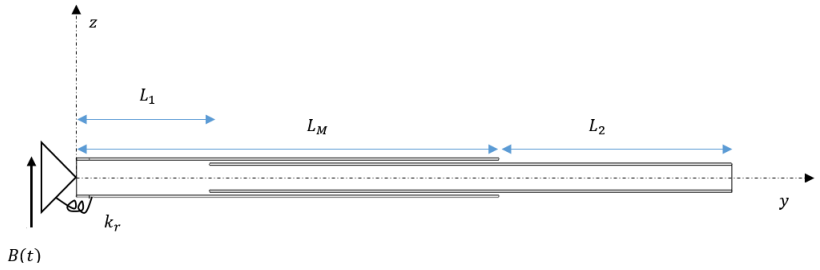

Figure 4.5: Gangway under base excitation

The equation of motion that describes the total displacement of the Ampelmann gangway is expressed as

$$\begin{cases} \rho A_M \frac{\partial^2 w_{t_1}}{\partial t^2} + (EI_{zz})_M \frac{\partial^4 w_{t_1}}{\partial y^4} + \left(\eta EI_{zz}\right)_M \frac{\partial^5 w_{t_1}}{\partial y^4 \partial t} = 0, & 0 \le y \le L_1(y) \\ \rho \left(A_M + A_T\right) \frac{\partial^2 w_{t_2}}{\partial t^2} + (EI_{zz})_{MT} \frac{\partial^4 w_{t_2}}{\partial y^4} + \left(\eta EI_{zz}\right)_{MT} \frac{\partial^5 w_{t_2}}{\partial y^4 \partial t} = 0, & L_1(y) \le y \le L_M \\ \rho A_T \frac{\partial^2 w_{t_3}}{\partial t^2} + (EI_{zz})_T \frac{\partial^4 w_{t_3}}{\partial y^4} + \left(\eta EI_{zz}\right)_T \frac{\partial^5 w_{t_3}}{\partial y^4 \partial t} = 0, & L_M \le y \le L_2(y) \end{cases} \tag{4.19}$$

The associated boundary condition of a moving support in the vertical z-axis at the base is as follow:

at $y = 0$

$$w_{t_1} = B(t) \qquad \text{and} \qquad \left(E + \eta E \frac{\partial}{\partial t}\right)(I_{zz})_M \frac{\partial^2 w_{t_1}}{\partial y^2} = k_r \frac{\partial w_{t_1}}{\partial y} \tag{4.20}$$

at $y = L$

$$\left(E + \eta E \frac{\partial}{\partial t}\right)(I_{zz})_T \frac{\partial^2 w_{t_3}}{\partial y^2} = 0 \qquad \text{and} \qquad \left(E + \eta E \frac{\partial}{\partial t}\right)(I_{zz})_T \frac{\partial^3 w_{t_3}}{\partial y^3} = 0 \tag{4.21}$$

The total transverse displacement w_{t_i} of any point along the beam can be written in terms of the elastic deflection w_i and the base excitation $B(t)$ and takes the following form:

$$w_{t_i} = w_i + B(t) \qquad \text{for} \quad i = 1,2,3 \tag{4.22}$$

Substituting Equation 4.22 in 4.19, 4.20 and 4.21 one can rewrite the partial differential equation and is given

as

$$\begin{cases} \rho A_M \frac{\partial^2 w_1}{\partial t^2} + (EI_{zz})_M \frac{\partial^4 w_1}{\partial y^4} + \left(\eta EI_{zz}\right)_M \frac{\partial^4 w_1}{\partial y^4} = -\rho A_M \frac{\partial^2 B}{\partial t^2}, & 0 \le y \le L_1(y) \\ \rho (A_M + A_T) \frac{\partial^2 w_2}{\partial t^2} + (EI_{zz})_{MT} \frac{\partial^4 w_2}{\partial y^4} + \left(\eta EI_{zz}\right)_{MT} \frac{\partial^4 w_2}{\partial y^4} = -\rho (A_M + A_T) \frac{\partial^2 B}{\partial t^2}, & L_1(y) \le y \le L_M \\ \rho A_T \frac{\partial^2 w_3}{\partial t^2} + (EI_{zz})_T \frac{\partial^4 w_3}{\partial y^4} + \left(\eta EI_{zz}\right)_T \frac{\partial^4 w_3}{\partial y^4} = -\rho A_T \frac{\partial^2 B}{\partial t^2}, & L_M \le y \le L_2(y) \end{cases} \tag{4.23}$$

The new boundary condition is sharing the same expression as in Equation 3.2 and 3.3.

Non-active motion compensation

The non-active compensation measured data along with its Fourier transform into frequency domain of the heave (vertical z-axis) motion is shown in Figure 4.9. The measured data is obtained with the Ampelmann system installed at the mid section of the vessel at an operational sea state condition of a significant wave height of 2.5m and a wave period of 7s. As can be seen the measured data represents a highly complex periodic

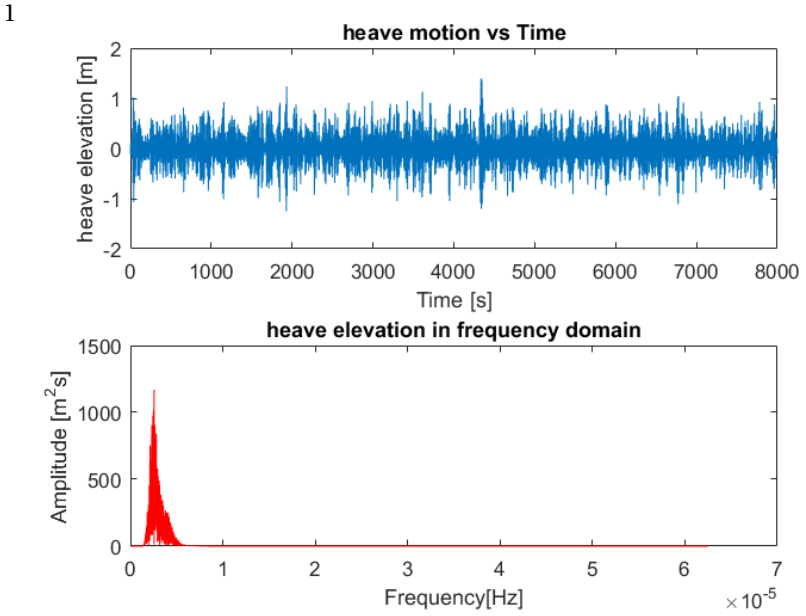

Figure 4.6: Measured Non-active motion compensation heave motion at the base

curve with finite number of individual sinusoidal waves and their related frequencies. In order to outline the base excitation, a simple sinusoidal function varying with time is applied to model the measured data. This model represents a continuous model to base excitation during non-active motion compensation. The base displacement $B(t)$ applied at base is written as

$$B(t) = \hat{B} \sin(\Omega_b t)$$

Differentiating the base displacement twice in time gives

$$B(t) = -\hat{B}\Omega_b^2 \sin(\Omega_b t)$$

The $\hat{B}$ is the amplitude of the base excitation and Ω_b is base excitation frequency.
From Figure 4.9, observe that the maximum heave amplitude is 1m at a base frequency of 0.2Hz. The dynamic response under sinusoidal base excitation of a fully extended gangway is shown in Figure 4.9.

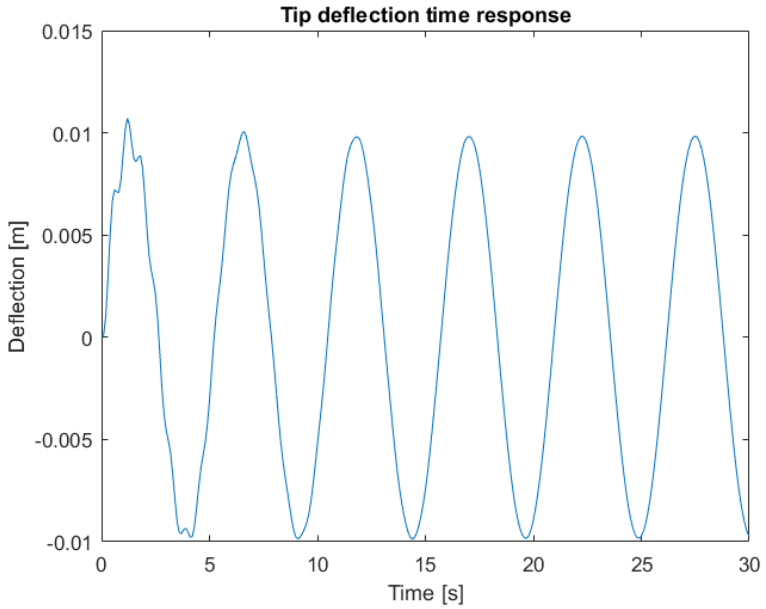

Figure 4.7: Tip deflection time response due to sinusoidal load

The result shows that the transient response of the gangway is damped out within four seconds and reached its steady state response. Since the steady state response last as long as the exciting force, for long term loading subject to large number of cycles may lead to fatigue failure.

Active motion compensation

During active motion compensation, the transfer deck cannot be kept completely motionless during operation. Due to the limited cylinders length of the Stewart platform, undesirable residual motion on the transfer deck (base) are present. These motion occurs randomly in time and served as pulse excitation to the system. Therefore, a sinusoidal model to predict these residual motion will not be valid. Instead a pulse base excitation for a impulse time interval of $0.5s$ is used to predict the dynamic response of the structure. A measured acceleration time response at the base of the gangway is given in Figure 4.8.

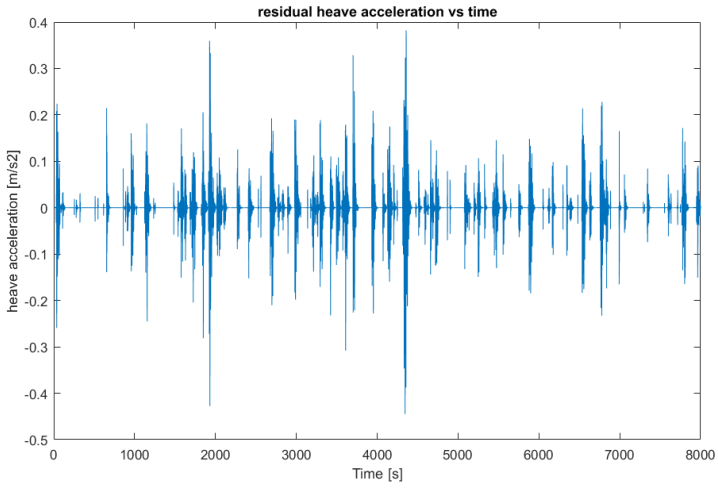

Figure 4.8: Measured heave acceleration at the base.

From the measured data, one can see that multiple impulse occurs during the time span. However, in this

analysis only the maximum impulse is used to determine to dynamics response of a fully extended gangway. The numerical results of the impulse response is shown in Figure 4.9

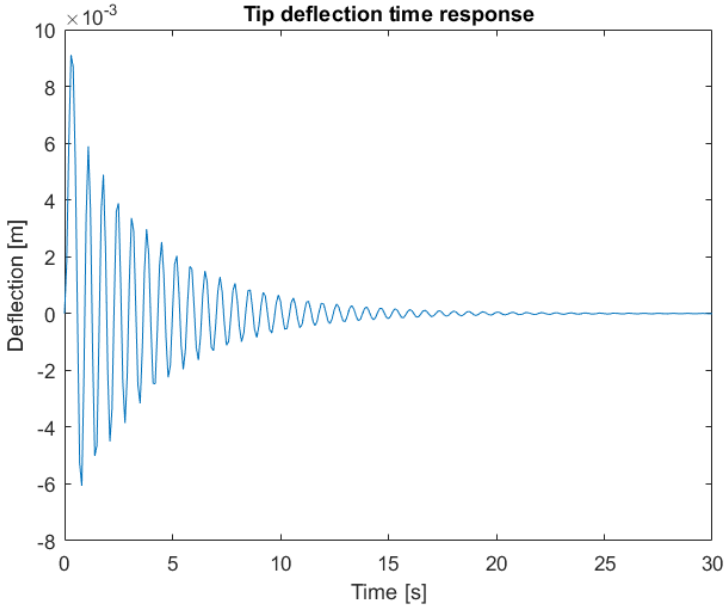

Figure 4.9: Tip deflection time response due to impulse load

4.3.2. Vibration under constant steady wind velocity

The Ampelmann system operates most of the time offshore where high wind velocity can occur. The G25 gangway is designed under a functional wind speed of $20\frac{m}{s}$. This wind condition is equivalent to Beaufort scale 7. The gangway is also able to withstand the wind under storm condition of $63\frac{m}{s}$. Wind on the surface of the earth is not constant in direction as well as in velocity. However, during analysis the wind velocity is assumed to be constant and the direction is always perpendicular to the gangway. As discussed previously, interaction between wind and the structure cause energy to dissipate due to there difference in velocity.
Consider the wind as a constant distributed force acting in the positive x-direction. The general form of the equation of motion that describes the bending motion of the gangway due to constant wind velocity is as follows:

$$\begin{cases} \rho A_M \frac{\partial^2 v_1}{\partial t^2} + (EI_{xx})_M \frac{\partial^4 w_1}{\partial y^4} + \left(\eta EI_{xx}\right)_M \frac{\partial^5 w_1}{\partial y^4 \partial t} + \rho A_M e \frac{\partial^2 \beta_1}{\partial t^2} = \frac{1}{2}\rho_{air} C_D L_{eff} \left(V_w^2 - 2v_W \frac{\partial v_1}{\partial t}\right), & 0 \le y \le L_1(y) \\ \rho (A_M + A_T) \frac{\partial^2 v_2}{\partial t^2} + (EI_{xx})_{MT} \frac{\partial^4 v_2}{\partial y^4} + \left(\eta EI_{xx}\right)_{MT} \frac{\partial^5 v_2}{\partial y^4 \partial t} + \rho (A_M + A_T) e \frac{\partial^2 \beta_2}{\partial t^2} = \frac{1}{2}\rho_{air} C_D L_{eff} \left(V_w^2 - 2V_w \frac{\partial v_2}{\partial t}\right), & L_1(y) \le y \le L_M \\ \rho A_T \frac{\partial^2 v_3}{\partial t^2} + (EI_{xx})_T \frac{\partial^4 v_3}{\partial y^4} + \left(\eta EI_{xx}\right)_T \frac{\partial^5 v_3}{\partial y^4 \partial t} + \rho A_M e \frac{\partial^2 \beta_3}{\partial t^2} = \frac{1}{2}\rho_{air} C_D L_{eff} \left(V_w^2 - 2V_w \frac{\partial v_3}{\partial t}\right), & L_M \le y \le L_2(y) \end{cases} \tag{4.24}$$

And for torsion vibration, the equation of motion is

$$\begin{cases} \left(I_{g_s}\right)_M \frac{\partial^2 \beta_1}{\partial t^2} - (GJ)_M \frac{\partial^2 \beta_1}{\partial y^2} - \left(\eta GJ\right)_M \frac{\partial^3 \beta_1}{\partial y^2 \partial t} + \rho A_M e \frac{\partial^2 v_1}{\partial t^2} = \frac{1}{2}\rho_{air} C_D e L_{eff} \left(V_w^2 - 2V_w \frac{\partial v_1}{\partial t}\right), & 0 \le y \le L_1(y) \\ \left(I_{g_s}\right)_{MT} \frac{\partial^2 \beta_2}{\partial t^2} - (GJ)_{MT} \frac{\partial^2 \beta_2}{\partial y^2} - \left(\eta GJ\right)_{MT} \frac{\partial^3 \beta_2}{\partial y^2 \partial t} + \rho A_{MT} e \frac{\partial^2 v_2}{\partial t^2} = \frac{1}{2}\rho_{air} C_D e L_{eff} \left(V_w^2 - 2V_w \frac{\partial v_2}{\partial t}\right)^2, & L_1(y) \le y \le L_M \\ \left(I_{g_s}\right)_T \frac{\partial^2 \beta_3}{\partial t^2} - (GJ)_T \frac{\partial^2 \beta_3}{\partial y^2} - \left(\eta GJ\right)_T \frac{\partial^3 \beta_3}{\partial y^2 \partial t} + \rho A_T e \frac{\partial^2 v_3}{\partial t^2} = \frac{1}{2}\rho_{air} C_D e L_{eff} \left(V_w^2 - 2V_w \frac{\partial v_3}{\partial t}\right), & L_M \le y \le L_2(y) \end{cases} \tag{4.25}$$

The interface and boundary condition required share the same expressions as stated in section 4.2.2. According to [3], wind processes in offshore environment are typically ten minutes for short term conditions. Taking the ten minutes as reference for wind exposure time, the fully extended gangway tip deflection and torsion displacement time history of the first fifty seconds for a steady wind velocity of $20\frac{m}{s}$ is shown in Figure 4.10.

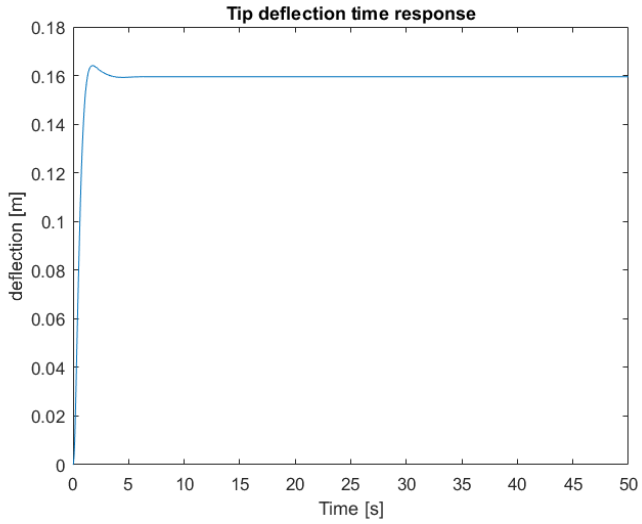

(a)

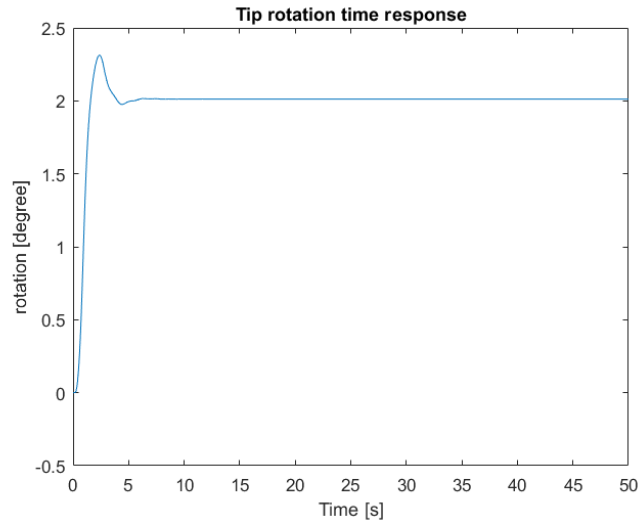

(b)

Figure 4.10: Bending and torsional vibration due to $20\frac{m}{s}$ wind velocity.

From the results it can be observed that little to no vibrations occur under a constant wind velocity of $20\frac{m}{s}$.

This occurs, because the gangway is highly damped due to the incorporated aerodynamic damping and also the time frame at which the wind is exposing is large.
To simulate the vibration of the gangway after the wind suddenly stops blowing, a exposing time duration of one second is chosen and the response of the gangway is given in Figure 4.11.

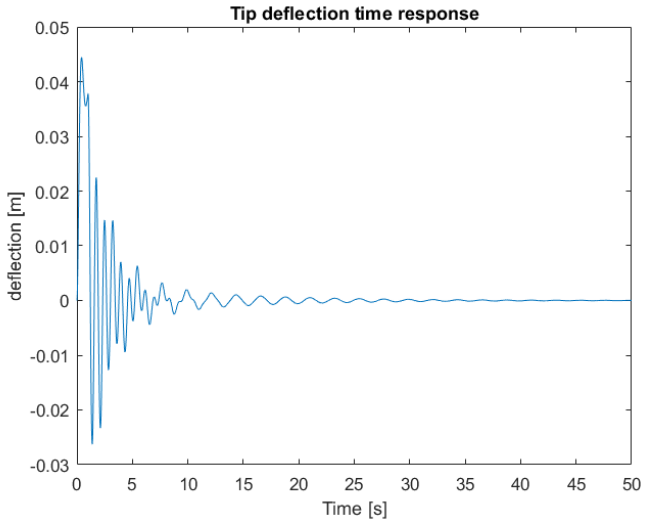

(a)

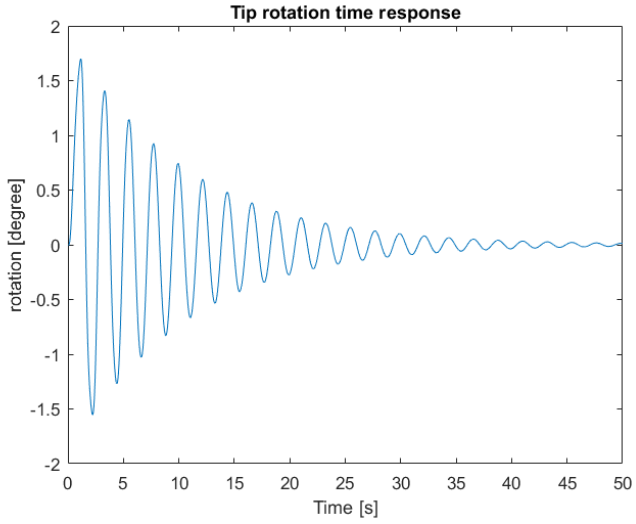

(b)

Figure 4.11: Bending and torsional vibration due to 20 $\frac{m}{s}$ wind velocity.

In case of a wind velocity of 63 $\frac{m}{s}$, the Ampelmann system will not be in operation according to Ampelmann basis of design [15]. Therefore, a three meter extension of the Gangway, which is typical during stowed condition is used. It is expected that the gangway will damped out swiftly and again a wind exposing for one second is used to analyze the dynamics. The time response is given in Figure 4.12.

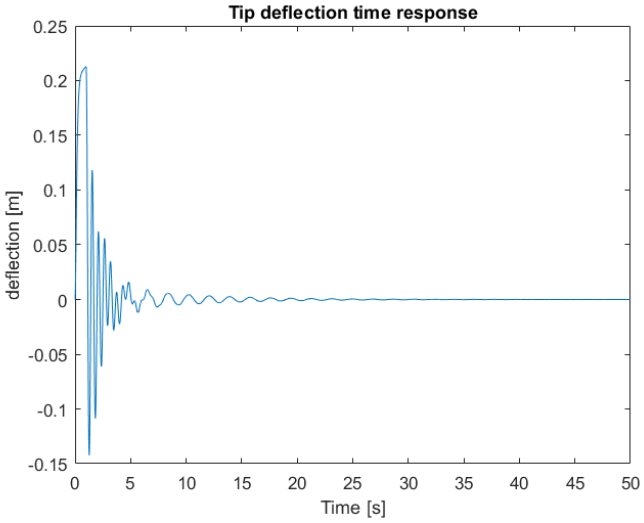

(a)

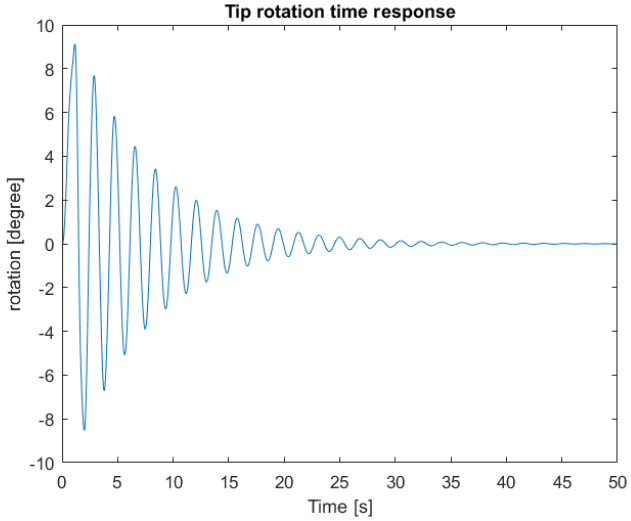

(b)

Figure 4.12: Bending and torsional vibration due to 63 $\frac{m}{s}$ wind velocity during 1s exposure.

4.4. Dynamic response to gangway maneuvers

As mentioned previously in the introduction, the gangway is a system that can move in three degrees of freedom (luffing, slewing and telescoping). Maneuvering the gangway is a random process that depends mostly on the operators steering the gangway and the situations they encounter. During analysis the gangway maneuvers are limited to the operations summed up in the following:

- Luff from $-20°$ to $0°$
- Slew from $0°$ to $90°$
- telescoping the gangway from minimum to maximum gangway length and vice versa

4.4.1. Vibration during luffing motion

Luffing motion describes the action of the gangway rotating around the x-axis, see Figure 4.13. Research in dynamic modeling a rotating beam are well presented nowadays. A model that is described in the most general way is published in [10]. In their model they take into account the stiffening and Coriolis effect due to the beam rotation. Those effects give rise to a coupling between axial and bending motion.

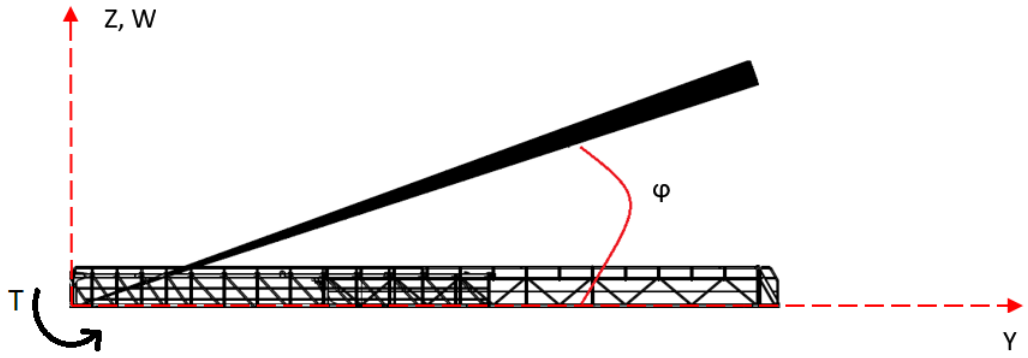

Figure 4.13: Luffing motion side view of the system.

However, these coupled effects have a great importance when a system, such as helicopter and aircraft turbine blade, is rotating at a high angular velocity.
In this study, the gangway is luffing at low angular rate and the contribution of the axial and Coriolis forces induced by the angular velocity are assumed to be insignificant to the system.
Consider the gangway is luffing under an applied torque T at the base shown with a mass moment of inertia I_{b_x} about the axis of rotation shown in Figure 4.13. Expression for the kinetic and potential energy of a small elastic deflection w in this situation is as follow:

$$E_{kin} = \frac{1}{2} I_{b_z} \left(\frac{\partial \phi}{\partial t}\right)^2 + \frac{1}{2} \int_0^L \rho A(y) \left(\frac{\partial w}{\partial t}\right)^2 + \rho A(y) y \left(\frac{\partial \phi}{\partial t}\right)^2 dy \tag{4.26}$$

$$E_{pot} = \frac{1}{2} \int_0^L \left(EI(y) \left[\frac{\partial^2 v}{\partial y^2}\right]\right)^2 dy \tag{4.27}$$

The work done for a given input torque is

$$W = T(t)\phi(t) \tag{4.28}$$

By applying the Hamilton's principle, $\delta \int_{t_1}^{t_2} \left(E_{kin} - E_{pot}\right) dt + \delta \int_{t_1}^{t_2} W = 0$, and then collecting all of the terms, yields a system equation of motion that describe a rotating gangway. The equation of motion of the segmented gangway with strain rate damping that result is given as follow:

$$\begin{cases} \rho A_M \frac{\partial^2 w_1}{\partial t^2} + (EI_{zz})_M \frac{\partial^4 w_1}{\partial y^4} + \left(\eta EI_{zz}\right)_M \frac{\partial^4 w_1}{\partial y^4} = -\rho A_M y \frac{d^2\varphi}{dt^2}, & 0 \le y \le L_1(y) \\ \rho (A_M + A_T) \frac{\partial^2 w_2}{\partial t^2} + (EI_{zz})_{MT} \frac{\partial^4 w_2}{\partial y^4} + \left(\eta EI_{zz}\right)_{MT} \frac{\partial^4 w_2}{\partial y^4} = -\rho (A_M + A_T) y \frac{d^2\varphi}{dt^2}, & L_1(y) \le y \le L_M \\ \rho A_T \frac{\partial^2 w_3}{\partial t^2} + (EI_{zz})_T \frac{\partial^4 w_3}{\partial y^4} + \left(\eta EI_{zz}\right)_T \frac{\partial^4 w_3}{\partial y^4} = -\rho A_T y \frac{d^2\varphi}{dt^2}, & L_M \le y \le L_2(y) \end{cases} \tag{4.29}$$

$$\left(E + \eta E \frac{\partial}{\partial t}\right) (I_{zz})_M \left.\frac{\partial^2 w_1}{\partial y^2}\right|_{y=0} + T - I_{b_x} \frac{d^2\varphi}{dt^2} = 0 \tag{4.30}$$

The associated boundary and interface conditions hold the same expression as given in Chapter 3.1.1.
The maximum torque that the luffing cylinders can deliver is 477 KNm and the rotational speed is restricted to 2.2$\frac{deg}{s}$ [15]. The maximum luffing torque however, is not the input torque to the system because the luffing cylinders are also used to carry the dead weight of the gangway. Subtracting the moment caused by the dead weight from the maximum torque gives the input torque during luffing. For a fully extended gangway the input torque is

$$T \approx 435 KNm$$

The target maneuver during luffing motion of the gangway is from $-20°$ to $0°$. The time needed to reach its target destination can be determined and is approximately 10s. Using this the torque input profile during luffing can be chosen for the system.
The torque input profile, as well as the numerical results of the dynamic response at the tip of fully extended gangway are shown in Figure 4.14 and 4.15 .

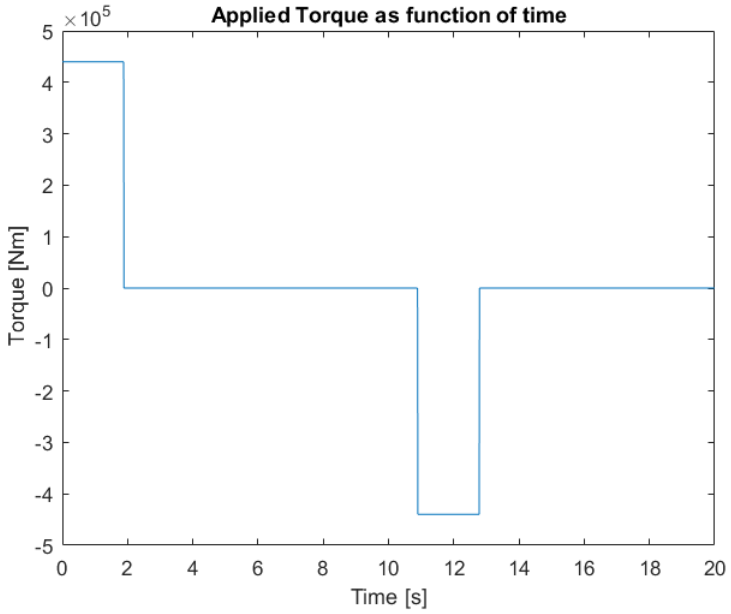

Figure 4.14: Input luffing torque applied at the base.

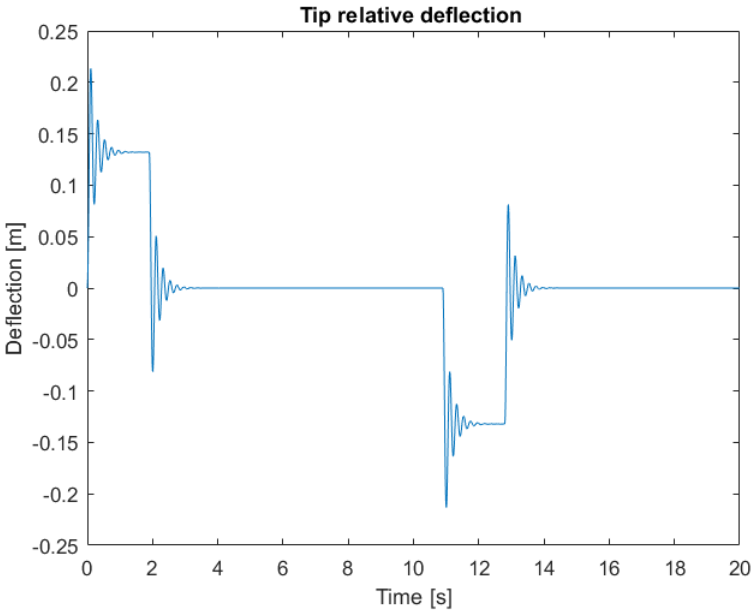

Figure 4.15: Transverse deflection during Luffing motion.

4.4.2. Vibration during slewing motion

Slewing motion describes the action of the gangway rotating around the z-axis. As discussed earlier, vibration in the x-y plane will induced torsional deflection. When the gangway is slewing under an applied torque, the rotating inertia of the gangway will also effect the torsional dynamics. A simple visualization of a rotating beam displaying coupled flexural and torsional vibration is shown in Figure 4.16. In Chapter 4.4.1 the equa-

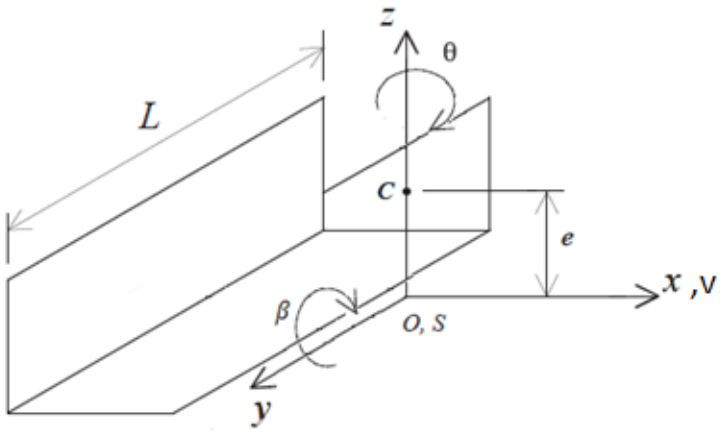

Figure 4.16: Slewing motion 3-D view.

tion of motion describing the bending vibration of a rotating gangway under an applied torque was stated. In this it can be observed that the rotational acceleration is explicit define as a forcing term at the right hand side of the equation of motion. Combining the effect of the rotating motion to the already defined coupled

bending-torsional equation, the equation of motion of gangway executing slewing motions become:

$$\begin{cases} \rho A_M \frac{\partial^2 v_1}{\partial t^2} + (EI_{xx})_M \frac{\partial^4 w_1}{\partial y^4} + \left(\eta EI_{xx}\right)_M \frac{\partial^5 w_1}{\partial y^4 \partial t} + \rho A_M e \frac{\partial^2 \beta_1}{\partial t^2} = \rho A_M y \frac{d^2\theta}{dt^2}, & 0 \le y \le L_1(y) \\ \rho (A_M + A_T) \frac{\partial^2 v_2}{\partial t^2} + (EI_{xx})_{MT} \frac{\partial^4 v_2}{\partial y^4} + \left(\eta EI_{xx}\right)_{MT} \frac{\partial^5 v_2}{\partial y^4 \partial t} + \rho (A_M + A_T) e \frac{\partial^2 \beta_2}{\partial t^2} = \rho (A_M + A_T) y \frac{d^2\theta}{dt^2}, & L_1(y) \le y \le L_M \\ \rho A_T \frac{\partial^2 v_3}{\partial t^2} + (EI_{xx})_T \frac{\partial^4 v_3}{\partial y^4} + \left(\eta EI_{xx}\right)_T \frac{\partial^5 v_3}{\partial y^4 \partial t} + \rho A_M e \frac{\partial^2 \beta_3}{\partial t^2} = \rho A_T y \frac{d^2\theta}{dt^2}, & L_M \le y \le L_2(y) \end{cases} \tag{4.31}$$

$$\begin{cases} \left(I_{g_s}\right)_M \frac{\partial^2 \beta_1}{\partial t^2} - (GJ)_M \frac{\partial^2 \beta_1}{\partial y^2} - \left(\eta GJ\right)_M \frac{\partial^3 \beta_1}{\partial y^2 \partial t} + \rho A_M e \frac{\partial^2 v_1}{\partial t^2} = \rho A_M e y \frac{d^2\theta}{dt^2}, & 0 \le y \le L_1(y) \\ \left(I_{g_s}\right)_{MT} \frac{\partial^2 \beta_2}{\partial t^2} - (GJ)_{MT} \frac{\partial^2 \beta_2}{\partial y^2} - \left(\eta GJ\right)_{MT} \frac{\partial^3 \beta_2}{\partial y^2 \partial t} + \rho A_{MT} e \frac{\partial^2 v_2}{\partial t^2} = \rho (A_M + A_T) e y \frac{d^2\theta}{dt^2}, & L_1(y) \le y \le L_M \\ \left(I_{g_s}\right)_T \frac{\partial^2 \beta_3}{\partial t^2} - (GJ)_T \frac{\partial^2 \beta_3}{\partial y^2} - \left(\eta GJ\right)_T \frac{\partial^3 \beta_3}{\partial y^2 \partial t} + \rho A_T e \frac{\partial^2 v_3}{\partial t^2} = \rho A_T e y \frac{d^2\theta}{dt^2}, & L_M \le y \le L_2(y) \end{cases} \tag{4.32}$$

$$\left(E + \eta E \frac{\partial}{\partial t}\right) (I_{zz})_M \left.\frac{\partial^2 w_1}{\partial y^2}\right|_{y=0} + T - I_{b_x} \frac{d^2\varphi}{dt^2} = 0 \tag{4.33}$$

where θ is the angle of rotation, I_{b_z} is the mass moment of inertia of the gangway about the z-axis.
The maximum input torque that the slewing motor can deliver and the restricted angular velocity during slewing according to [15] is $318 KNm$ and $10 \frac{deg}{s}$. The target maneuver during slewing is from 0° to 90°. Using the restricted angular velocity, the action can be reach in $10 s$ and with this the torque profile can be composed.
The results of the displacement time history representing the tip deflection and torsional displacement during slewing with its torque input profile are shown in 4.17, 4.18 and 4.19.

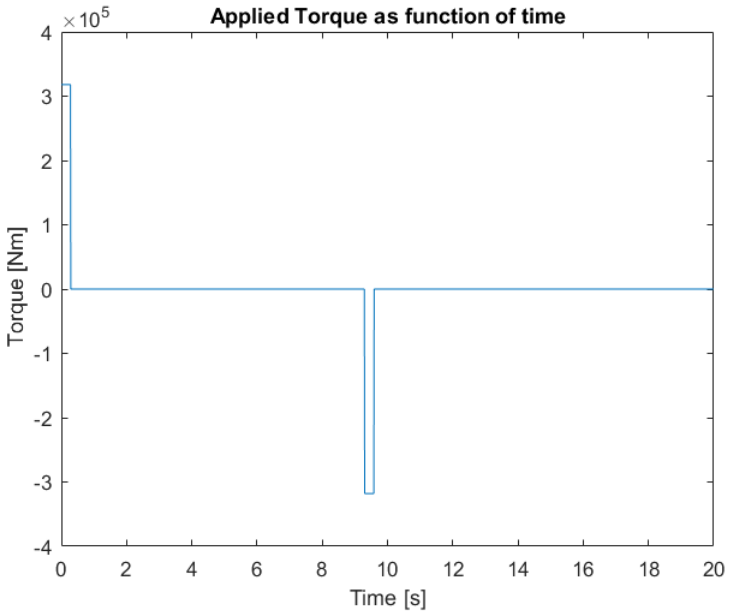

Figure 4.17: Input Slewing torque applied at the base.

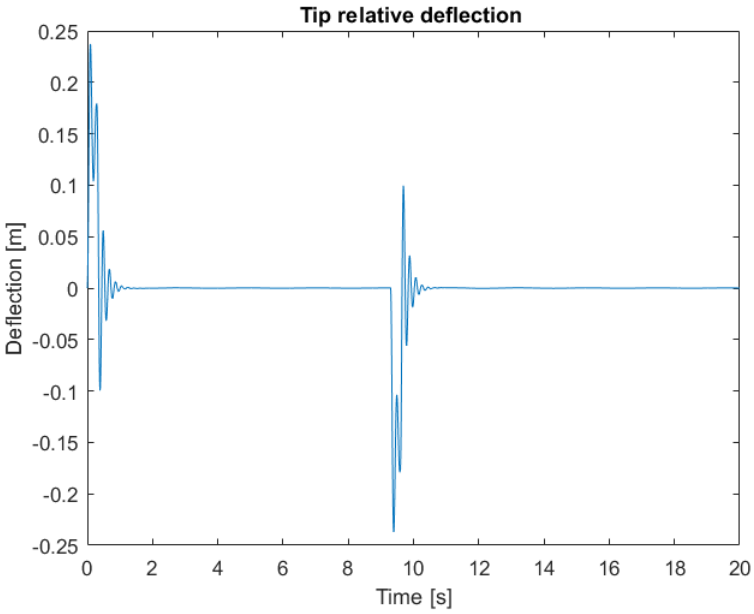

Figure 4.18: Transverse deflection during slewing motion.

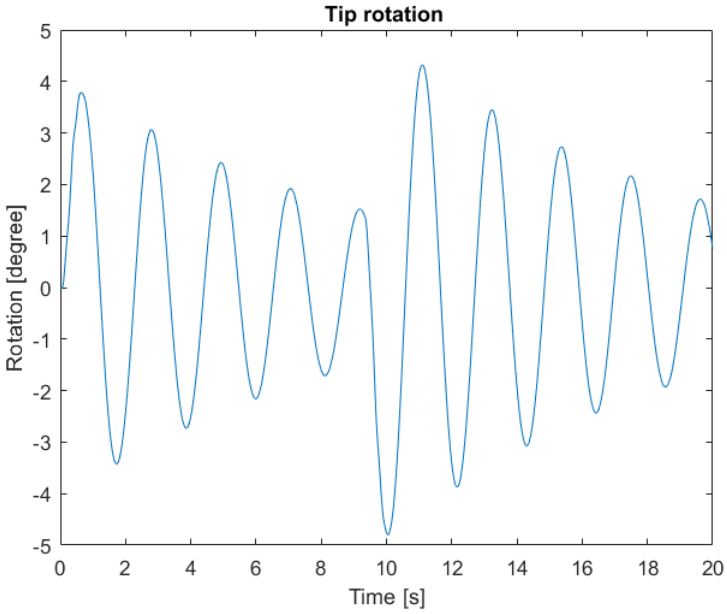

Figure 4.19: Torsional deflection during slewing motion.

4.4.3. Vibration during telescoping motion

Application to axially moving beam describes the telescoping action of the T-boom. Early studies on the dynamics of moving particles in a beam were conducted with fluid in a pipe. In terms of mathematics, modeling the dynamics of a beam whose length is time dependent manifest some aspects of a pipe conveying fluid problem. Authors of [4] found the dynamic equation of motion that give a detailed account on the transverse vibration of an axially moving beam. They presented a theoretical model imposing the assumptions which are essential for Euler-Bernoulli beam theory.

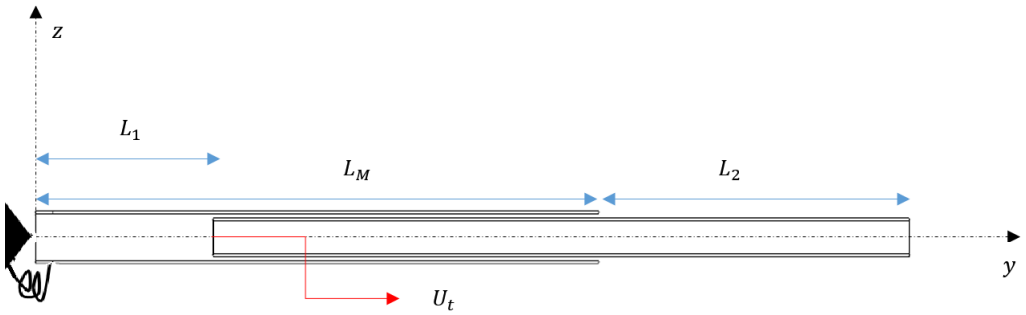

Figure 4.20: Telescoping motion.

Consider a T-boom moving axially from the Main boom with a constant velocity represented in Figure 4.20. The forces due to the moving T-boom in transverse direction consist of two elements, namely 1) Coriolis force and 2) Centrifugal force. The expression of the two elements are given in the equations below:

$$F_{coriolis} = 2\rho A_T U_t \frac{\partial^2 w}{\partial y \partial t} \tag{4.34}$$

$$F_{centrifugal} = \rho A_T U_t^2 \frac{\partial^2 w}{\partial y^2} \tag{4.35}$$

Where, A_T is the cross sectional area of the T-boom and U_t is the constant telescoping velocity. If one assume that the bending displacement w_1, w_2 and w_3 corresponds to the boundary of $0 \leq y \leq L_1(y)$, $L_1(y) \leq y \leq L_M$ and $L_M \leq y \leq L_2(y)$ respectively, the dynamic equation of motion that define the vibration due to the moving T-boom can be readily obtained by adding the two forces to the Euler-Bernoulli beam model. The expression for the transverse vibration of the Main and T-boom is as follows:

$$\begin{cases} \rho A_M \frac{\partial^2 w_1}{\partial t^2} + (EI_{zz})_M \frac{\partial^4 w_1}{\partial y^4} = 0, & 0 \leq y \leq L_1(y) \\ \rho (A_M + A_T)) \frac{\partial^2 w_2}{\partial t^2} + (EI_{zz})_{MT} \frac{\partial^4 w_2}{\partial y^4} + 2\rho A_T U_t \frac{\partial^2 w_2}{\partial y \partial t} + \rho A_T U_t^2 \frac{\partial^2 w_2}{\partial y^2} = 0, & L_1(y) \leq y \leq L_M \\ \rho A_T \frac{\partial^2 w_3}{\partial t^2} + (EI_{zz})_T \frac{\partial^4 w_3}{\partial y^4} + 2\rho A_T U_t \frac{\partial^2 w_3}{\partial y \partial t} + \rho A_T U_t^2 \frac{\partial^2 w_3}{\partial y^2} = 0, & L_M \leq y \leq L_2(y) \end{cases} \tag{4.36}$$

It should be noted that a positive and negative telescoping velocity U_t prescribe the instantaneous extension and retraction of the gangway. The interface condition at every time instance should satisfy the continuity and momentum balance and this was already mentioned in Chapter 3.1.1. During operation Ampelmann is extended or retracted at a constant telescoping velocity $U_t = 1\frac{m}{s}$ [15]. The prescribed motion profile for simulating the telescoping motion of the gangway is

$$L(t) = U_t t$$

In order to simulate the transient response during extending or retracting, the initial displacement is set to be equal to the static deflection of the gangway.
For an extending gangway from fully retracted to fully extended event the result is given in Figure 4.21. When the procedure is reversed, the retracting gangway tip deflection response is given in Figure 4.22.

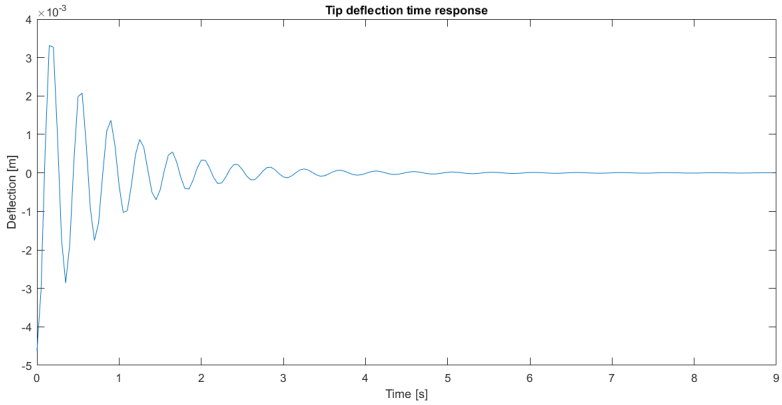

(a) Tip deflection with damping in the system.

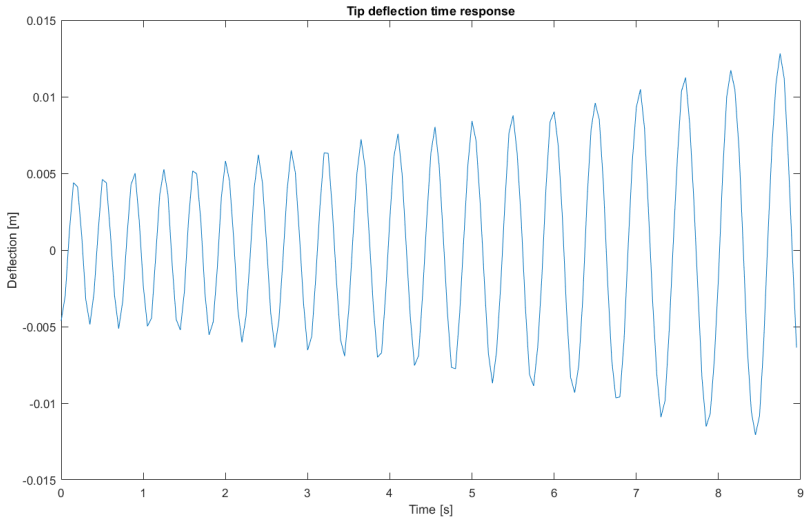

(b) Tip deflection without damping in the system

Figure 4.21: Tip deflection during extension

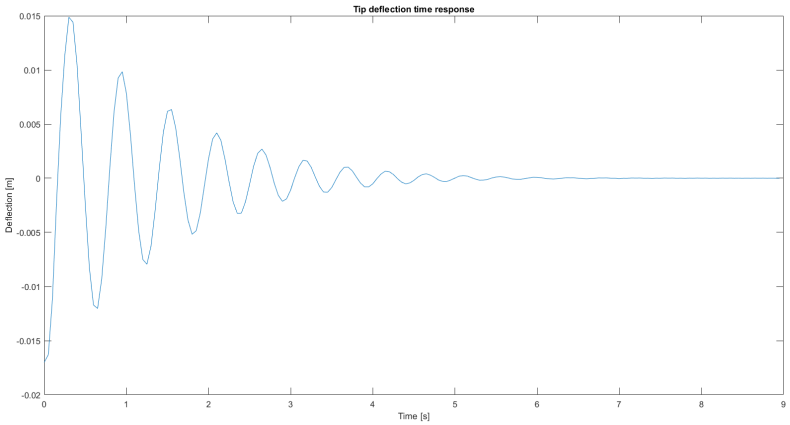

(a) Tip deflection with damping in the system.

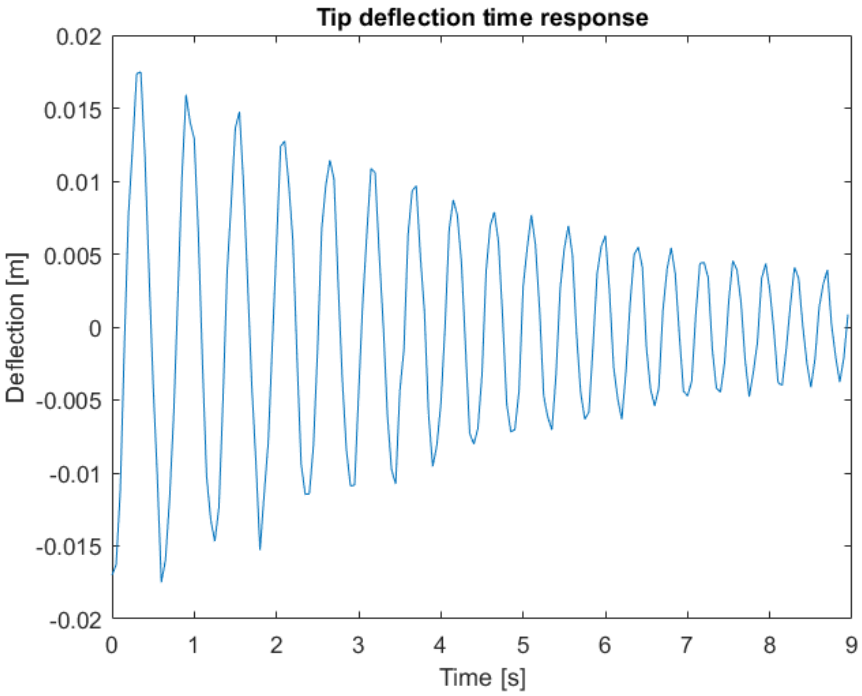

(b) Tip deflection without damping in the system

Figure 4.22: Tip deflection during retraction

5

Fatigue Analysis

The objective in this section is to provide a fatigue analysis on the Ampelmann G25 gangway based S-N curve approach. Various dynamic condition were presented in the previous section, however, not all design cases will be considered in the fatigue life analysis. In section 5.1 a summary of the design load cases is provided to determine the fatigue life of the gangway. The bending stress time conversion to the already obtained displacement time response is discussed in Chapter 5.2. Chapter 5.3 introduces the fatigue damage calculation according to Miner's rule. In this also the S-N curve and stress counting method was selected and is given in Chapter 5.4 and Chapter 5.5 receptively. Finally in Chapter 5.6 provides the analysis results and fatigue life based on Miner's rule.

5.1. Fatigue design load case

Dynamic analysis were investigated in the previous chapter. Although, dynamic analysis under external disturbance were made, estimating the fatigue life under these conditions are not considered.
The main interest is the fatigue life due to maneuvers of the gangway. The load case to be assessed on the Ampelmann G25 gangway are the steps during the operational maneuvers. A typical maneuvering operational load cycle is defined in the following:

- Luff from -20° to 0°.
- Slew from 0° to 90° .
- Slew from 90° to 0°.
- Luff from 0° to -20°

For these operational cycle the most extreme case is considered. This is when the gangway is in fully extended configuration where the bending stresses are the highest at the base.

5.2. Bending stress time history

Fatigue analysis deal with stress level in a material. The results obtained from the dynamic analysis are displacement over time series at any arbitrary point in the gangway. Conversion from displacement-time history to stress-time history is required. The relation between transverse displacement and the normal stress at any point on the gangway can be determined from the the local bending moment and is expressed by following equation

$$\sigma(y,t) = \frac{M(y,t)z}{I_{zz}} \tag{5.1}$$

The parameter σ is the normal stress, M is the bending moment, z is the distance to the neutral axis of the cross section and I_{zz} is the second moment of inertia in the z-axis. Since the normal stress varies linearly on a cross section, the maximum stress occurs at the outer surface of the gangway where the distance z is the largest.
By substituting the relation between the bending moment and the transverse displacement, $M(y,t) = EI_{zz}\frac{\partial^2 w(y,t)}{\partial y^2}$, in the normal stress relation, one can rewrite the equation as

$$\sigma(y,t) = EI_{zz}\frac{\partial^2 w(y,t)}{\partial y^2}\frac{z}{I_{zz}} \tag{5.2}$$

Again by applying the shape functions discussed in Chapter 2.3 to the normal stress relation and carry out the differentiation, one can obtain the normal stress relation along the length of an element as

$$\sigma(y,t) = \frac{EI_{zz}.z}{I_{zz}}\left[\left(\frac{12y}{l_e^3} - \frac{6}{l_e^2}\right)w_i + \left(\frac{6y}{l_e^2} - \frac{4}{l_e}\right)\theta_i + \left(\frac{6}{l_e^2} - \frac{12y}{l_e^3}\right)w_j + \left(\frac{6y}{l_e^2} - \frac{2}{l_e}\right)\theta_j\right] \tag{5.3}$$

Observe that Equation 5.3 is written in finite element form. The nodal values, $w_{i,j}$ and $\theta i, j$, are known constants obtained from displacement-time history.
One should note that the stress relation share the same form as in the vertical z-axis as well as in the horizontal x-axis.

5.3. Palmgren-Miner rule

The Palmgren-Miner rule or simply the Miner's rule is most widely used cumulative damage model to determine the fatigue life of a system. The Miner's rule assume a linear cumulative damage model that determines the damage done by each cyclic load is expressed as

$$damage = \sum_{i=1}^{k}\frac{n_i}{N_i} \tag{5.4}$$

In this equation, n_i represents the the number of cycles at each stress block k and N_i is the numbers of cycles to failure or fatigue capacity on each stress level.

5.4. S-N curve

Engineering fatigue data of a material is normally constructed by experimenting a specimen under cyclic loading. The number of cycles to failure of each stress level are represented by means of a S-N curve. The S-N curve can be approximated by the Basquin relation given as

$$S_a^k N = a \tag{5.5}$$

To this S_a is the stress amplitude range, N is the fatigue cycles capacity, k is the negative inverse slope of the S-N curve and a is intercept of the design S-N curve.
The fatigue design parameters used in this research is based on the data of structural class B1 of [2].
A summary of the design values is given in table 5.1. It should be noted that both k and a are parameters which depends on the material and welding features.

Table 5.1: Fatigue analysis parameters

Design values	
k	4
$\log a$	15.117

5.5. Stress Counting

Complex load histories requires stress counting procedure to compute the number of cycles of each stress level. The most common technique to extract the number of stress reversal from a of stress time series under different amplitudes is by using the rainflow counting method. The rainflow counting method captures the number cycles at each stress level, this is needed in order to asses the fatigue damage according to Miner's rule.
The Procedure for rainflow cycle counting is given is summarized as follows:

1. Rotate the stress-time history 90° such that the time axis vertically downward with starting time at the top, resembling a roof.

2. Imagine each peak with a rain flow dripping down.

3. Counting half cycles by allowing the flow to continue drips down the roof and looking for flow termination. This occurs when either:

   - it falls below the roof meaning that it reaches the end of the time history.
   - it intercepts with the previous flow from above.

4. Identify each cycle by pairing up half cycles with identical magnitudes and count the number of complete cycles.

5.6. Fatigue life estimation

As said earlier the fatigue life is estimated in terms of number of operational maneuvers. One should note that no friction forces were present in the setup of the equation of motion at the boundary, a counter torque is needed to stop the gangway from rotating. Each motion causing a fatigue loading to the gangway is analyzed and implemented in the calculation. To evaluate the fatigue life of each component, calculations are done in the following order:

1. Obtain the displacement time history during dynamic analysis (see Chapter 3).

2. Convert the displacement time history to stress time history using Equation 5.3.

3. Predict the number cyclic loading over the time period according Chapter 5.5

4. Evaluate the fatigue damage done to the system using Miner's rule.

The obtained stress time history, stress counts and fatigue damage of each profile are given in below.

Luffing motion results

1. *Stress time history.*
   The converted luffing stress time history from $-20°$ to $0°$ with maximum luffing velocity $2.2\frac{deg}{s}$ can be seen is shown in Figure 5.1.

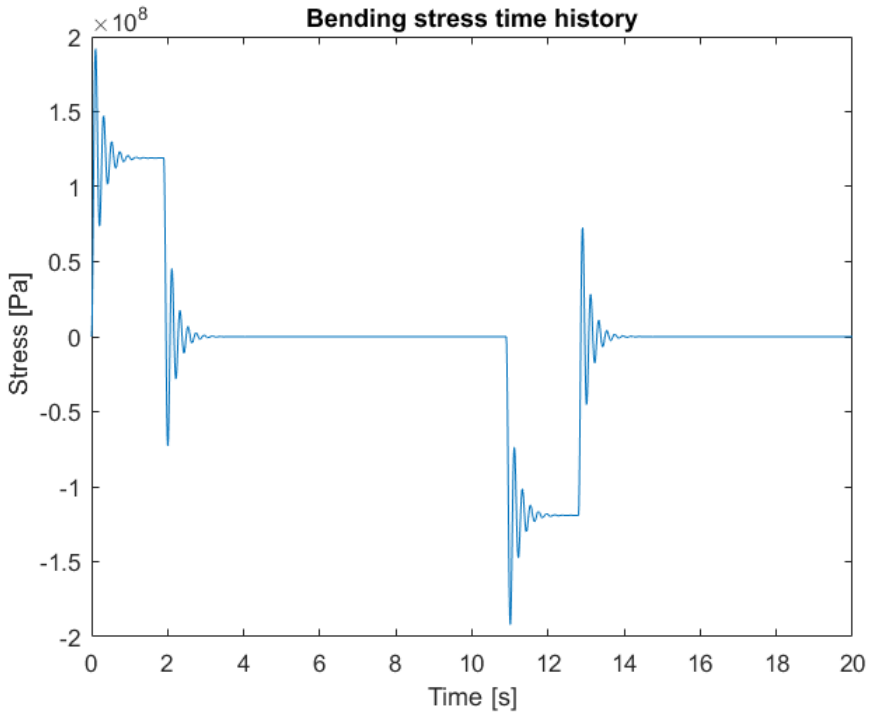

Figure 5.1: Stress time history during luffing motion

2. *Stress cycle counts.*
   In Figure 5.2, one can see the histogram obtained using rainflow analysis to count the number of stress cycles.

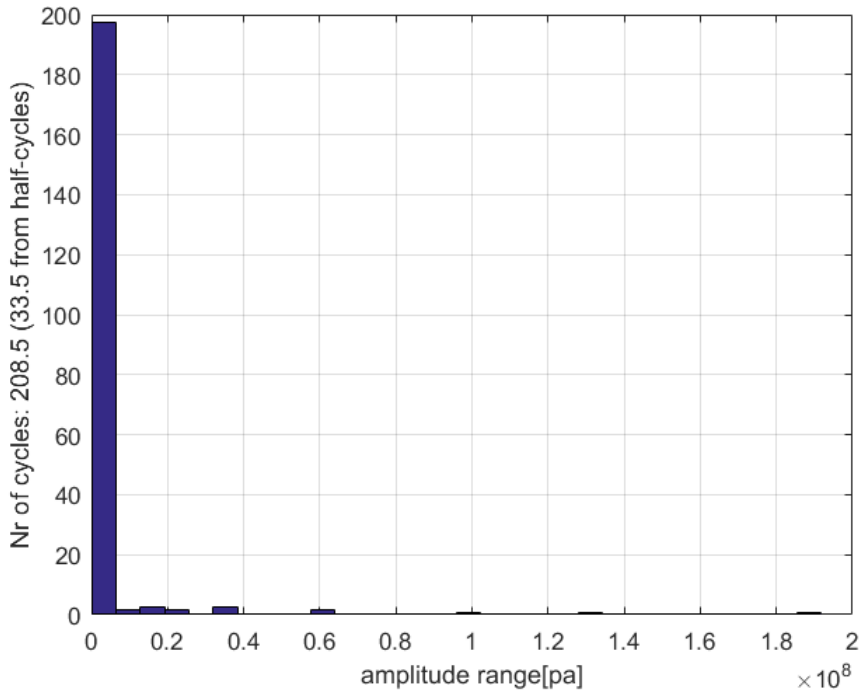

Figure 5.2: Histogram stress cycles during luffing operation

3. *Fatigue damage*
   The fatigue damage for the luffing motion from $-20°$ to $0°$ is

$$damage = 4.9996 \cdot 10^{-7}$$

Since the luffing motion from $0°$ to $-20°$ is having the same luffing velocity of $2.2\frac{deg}{s}$. It is safe to say that the stress time response is fully reversed while sharing the same number of stress counts when gravity is neglected. Therefore, the damage done is also having the same value.

Slewing motion results

1. *Stress time history*
   In Figure 5.3 the stress time history during slewing motion from $0°$ to $90°$ with maximum slewing velocity $10\frac{deg}{s}$

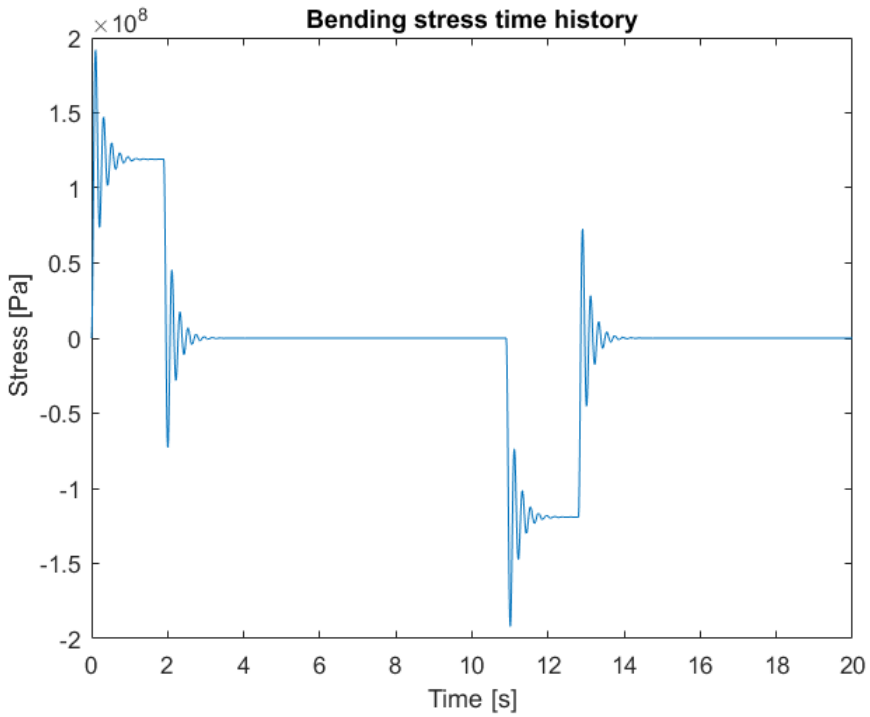

Figure 5.3: Stress time history during slewing motion

2. *Stress cycle counts.*
   The corresponding stress cycle count can be seen in Figure 5.4.

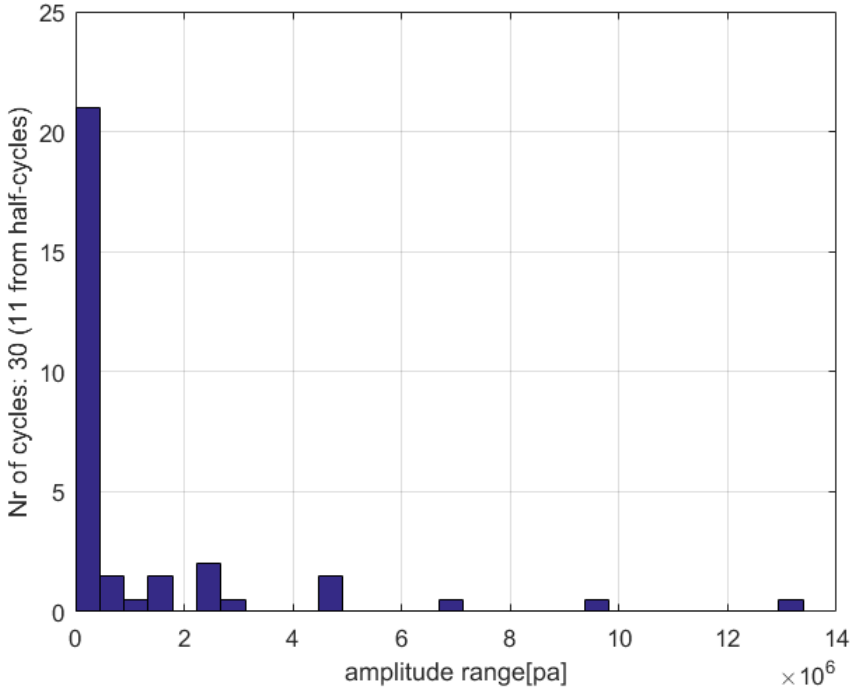

Figure 5.4: Histogram stress cycles during slewing operation

3. *Fatigue damage*
   The fatigue damage for the slewing motion from 0 to 90 deg is

$$damage = 1.7742 \cdot 10^{-10}$$

Again, for slewing motion from 90° to 0°, the cycles are fully reversed and the damage to the structure is equal.

Fatigue life

The expected Fatigue life can be evaluated using Miner's rule. According to the Miner's rule, failure will occur when the damage reaches to the value of one. In mathematical terms it is expressed as

$$\sum damage = 1 \tag{5.6}$$

The damage done per slewing and luffing cycle were already obtained and the expected fatigue life in number of operation cycles can be determined with the following equation

$$\text{Fatigue Life} = \frac{1}{\sum damage} \tag{5.7}$$

A summary of the obtained fatigue damage is given in Table 5.2.

Table 5.2: fatigue damage summary

Component	damage
luff -20 to 0	$4.9996 \cdot 10^{-7}$
slew 0 to 90 deg	$1.7742 \cdot 10^{-10}$
slew 90 to 0 deg	$1.7742 \cdot 10^{-10}$
luff 0 to -20	$4.9996 \cdot 10^{-7}$
Total	$\approx 10^{-6}$

The estimated fatigue life in number of maneuvering cycles is

$$\text{Fatigue Life} \approx 10^{6} \quad \text{maneuvering cycles}$$

The influence of the material damping value to the fatigue life were conducted. A comparison for the fatigue life with two different damping parameters can be seen in Table 5.5.

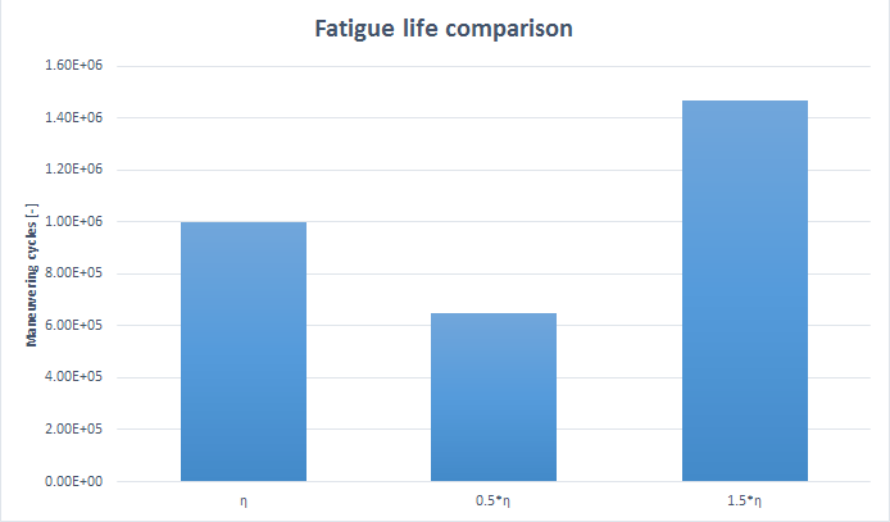

Figure 5.5: Histogram stress cycles during slewing operation

6

Conclusion and Recommendation

Conclusion

In this thesis a dynamic model for the Ampelmann G25 gangway was developed in bending and coupled bending-torsional motion. The structural mathematical model is based on Euler-Bernoulli hypothesis including strain rate damping to describe the vibrations. Finite element method was implemented to reproduce the dynamics of the G25 gangway to external disturbance and gangway maneuvers.

The log decrement method was used to determine the damping parameter from the measured data. Comparing the test data to the free vibration analysis obtained using Euler-Bernoulli beam mathematical model shows sufficiently accurate results in the vertical direction. The natural frequencies depends mostly on the stiffness, mass and the boundary condition of the gangway. Additionally, the extension length of the gangway is also a main contributing factor: the longer the extension leads to a less stiff structure thereby lowering the natural frequency. The natural frequency found in the horizontal x-axis is quite low. This is because the first mode vibrates at the first torsional natural frequency.

The dynamic behavior under steady wind velocity shows that for high wind velocity, the gangway is highly damped due to the incorporated aerodynamic damping to the system. However, this is only the case when wind exposure time is infinite. Furthermore, the response shows that bending vibration damps out faster that torsional vibration.
The dynamic behavior under base excitation were modeled in two ways: a sinusoidal model and a pulse excitation model. The sinusoidal model represents the continuous motion subjected the hexapod and it was found that the gangway under maximum working sea state condition, the excitation frequency is swiftly damped out and the steady state is reached. The pulse excitation model was used to simulate residual motion and the results show more abrupt vibrations compared to the sinusoidal model.
In telescoping of the gangway it was observed that the period of vibration increases during extension and decreases during retraction. This is the effect of the changing length and mass system.
Research in fatigue analysis under gangway maneuvers were conducted. The maneuvers are slewing and luffing motion of the gangway. The results in fatigue analysis indicates it can withstand up to 10^6 operational maneuvers for a typical maneuver profile. To this, the dominant factor to fatigue is the luffing motion. However, this might not be the case when warping is added to the equation of motion which might effect the stress cycles in during slewing.
Deviating the maneuver profile and adjusting the input torque given in the analysis may lead to a different fatigue life.

Recommendation

The most important recommendation is to verify the dynamic model through experimental measurements. In this model, the damping parameter in torsional vibration was taken as the same value used in bending vibration. The energy dissipation in torsion may be different then in bending. Also, from the free vibration test that have been carry out, the decay shows a rough decay. This might indicate that other damping mechanisms are involved in the system. Conducting more measurements allow one to develop a better overall damping of the gangway in bending as well as in torsion.

The gangway model using Euler-Bernoulli beam theory can describe the dynamics of the G25 gangway. Many assumptions were made in obtaining the dynamic response especially in the coupled bending-torsional vibration and external loads.
For future research in terms of the improvement of dynamic model one may include:

- The combination maneuvering (luffing, slewing and telescoping) effect. In this thesis all those maneuvers were investigated separately and does not represent a real life situation where the operator handles those maneuvers at once.
- A dynamic wind load to the structure for a better understanding of wind induced vibration. Wind forces on structures are unsteady due to the alteration in aerodynamic forces, vortex shedding and wind gust. The cyclic frequency of the aerodynamic forces may coincide with a natural frequency of the gangway.
- Spring stiffness to the interfaces between the overlapping area of the main and T-boom. The equilibrium in forces and continuity in displacement and rotation at the interfaces assumed in this thesis are not fully correct. In between the interface there are wheels attached to allow the T-boom to telescope forward and backward. During bending in the vertical direction the transfer of forces at the interfaces may not be constant.
- The warping effect of the gangway. The gangway is an 'U shape' like beam where warping will occur during torsional vibration. Including warping effect will decrease the natural frequency of the gangway.

A

Ampelmann gangway system

In this appendix some additional information is presented on the gangway system are given.

A.1. Gangway G25 parameters

The Ampelmann G25 gangway parameters are given here in this section.

Symbol	Description	value
m_M	Mass main boom	$2181kg$
m_T	Mass main boom	$1365kg$
ρ	Steel density	$7800\frac{kg}{m^3}$
C_D	Drag coefficient	1.65
E	Young's modulus	$210\cdot10^9Pa$
G	Shear modulus	$46\cdot10^9Pa$
I_{g_M}	Mass moment of inertia main boom	$10288kg\cdot m^2$
I_{g_M}	Mass moment of inertia T-boom	$8282kg\cdot m^2$
I_{xx_M}	Second moment of inertia in x-axis	$0.0012m^4$
I_{xx_T}	Second moment of inertia in x-axis	$7.5134\cdot10^{-4}m^4$
I_{zz_M}	Second moment of inertia in z-axis	$0.0018m^4$
I_{zz_T}	Second moment of inertia in z-axis	$9.7030\cdot10^{-4}m^4$
J_M	Torsional constant	$2.265\cdot10^{-5}m^4$
J_T	Torsional constant	$1.72\cdot10^{-5}m^4$
k_r	Rotational spring stiffness	$2\cdot2.07\cdot10^8\frac{N\cdot m}{rad}$
L_M	Main boom length	$12.9m$
L_T	T-boom length	$13.2m$
L_Te	Total extension length	$25m$

L_r	Total retracted length	$16m$

A.2. Ampelmann placement on the ship

The Ampelmann placement on a vessel is installed at the midships, port side as shown Figure A.1. The wave direction is 135° with a significant wave height of $1.5m$ and a wave period of $7s$

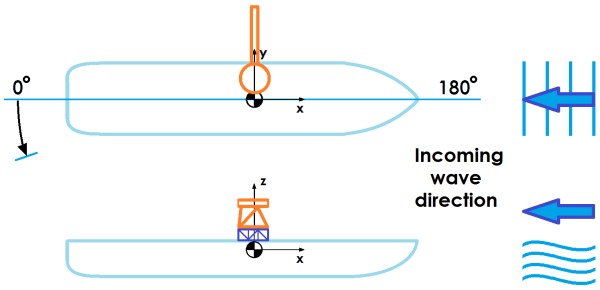

Figure A.1: Ampelmann placement

A.3. General operation procedure

The step by step operational procedure for the Ampelmann system can be seen in Figure A.2.

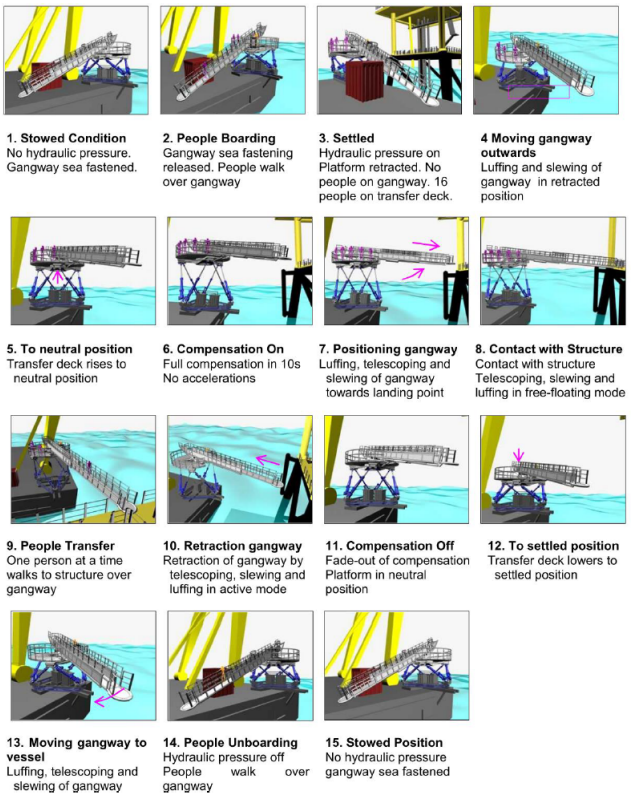

Figure A.2: Operational procedure

B

Numerical Method

As discussed in Chapter 4.1 the finite element method was used to solve for the partial differential equations.

B.1. Finite element Method

Consider a beam discretized in two elements with a rotation spring k_r boundary at the left side as shown in Figure B.1. Each element is of length l_e with an cross sectional area A, a density ρ and a flexural rigidity EI. The mass and stiffness matrix of each element is given as follow:

$$[M_1] = \frac{\rho A l_e}{420}\begin{bmatrix} 156 & 22l_e & 54 & -13l_e \\ 22l_e & 4l_e^2 & 13l_e & -3l_e^2 \\ 54 & 13l_e & 156 & -22l_e \\ -13l_e & -3l_e^2 & -22l_e & 4l_e^2 \end{bmatrix} \qquad [M_2] = \frac{\rho A l_e}{420}\begin{bmatrix} 156 & 22l_e & 54 & -13l_e \\ 22l_e & 4l_e^2 & 13l_e & -3l_e^2 \\ 54 & 13l_e & 156 & -22l_e \\ -13l_e & -3l_e^2 & -22l_e & 4l_e^2 \end{bmatrix}$$

$$[K_1] = \frac{EI}{l_e^3}\begin{bmatrix} 12 & 6l_e & -12 & 6l_e \\ 6l_e & 4l_e^2 & -6l_e & 2l_e^2 \\ -12 & -6l_e & 12 & -6l_e \\ 6l_e & 2l_e^2 & -6l_e & 4l_e^2 \end{bmatrix} \qquad [K_1] = \frac{EI}{l_e^3}\begin{bmatrix} 12 & 6l_e & -12 & 6l_e \\ 6l_e & 4l_e^2 & -6l_e & 2l_e^2 \\ -12 & -6l_e & 12 & -6l_e \\ 6l_e & 2l_e^2 & -6l_e & 4l_e^2 \end{bmatrix}$$

The next step is to form the global matrix to represent the total system of the beam. The mass and stiffness element matrix is assembled into a global inertia matrix $[\boldsymbol{M}]$ and a structural stiffness matrix $[\boldsymbol{K}]$ with $2(N+1)$

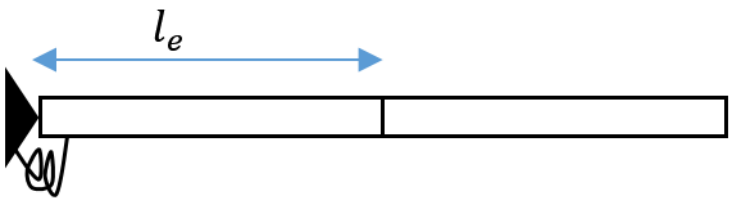

Figure B.1: Two element beam

degrees of freedom for pure bending beam. Using finite element method the interface condition will be naturally satisfied when constructing the system mass and stiffness matrices.
The global finite element mass and stiffness matrix is as follow:

$$\boldsymbol{M} = \frac{\rho A l_e}{420}\begin{bmatrix} 156 & 22l_e & 54 & -13l_e & 0 & 0 \\ 22l_e & 4l_e^2 & 13l_e & -3l_e^2 & 0 & 0 \\ 54 & 13l_e & 312 & 0 & 54 & -13l_e \\ -13l_e & -3l_e^2 & 0 & 8l_e^2 & 13l_e & -3l_e^2 \\ 0 & 0 & 54 & 13l_e & 156 & -22l_e \\ 0 & 0 & -13l_e & -3l_e^2 & -22l_e & 4l_e^2 \end{bmatrix}$$

$$\boldsymbol{K} = \frac{EI}{l_e^3}\begin{bmatrix} 12 & 6l_e & -12 & 6l_e & 0 & 0 \\ 6l_e & 4l_e^2 & -6l_e & 2l_e^2 & 0 & 0 \\ -12 & -6l_e & 24 & 0 & -12 & 6l_e \\ 6l_e & 2l_e^2 & 0 & 8l_e^2 & -6l_e & 2l_e^2 \\ 0 & 0 & -12 & -6l_e & 12 & -6l_e \\ 0 & 0 & 6l_e & 2l_e^2 & -6l_e & 4l_e^2 \end{bmatrix}$$

The next step is to apply the boundary condition to the nodal displacement and rotation. Referring node one to be at the base, the displacement is zero and this essential boundary condition can be eliminated by canceling out the first degree of freedom. The natural boundary condition at node one however, depends on the rotation spring stiffness at the base. One can leave it as a load vector or simply add the rotational stiffness to global stiffness matrix at the second degree of freedom of node one. At the free end the homogeneous natural boundary condition is implicitly contained.
Applying the essential and natural boundary conditions to the global finite element matrices takes the following form:

$$\boldsymbol{M} = \frac{\rho A l_e}{420}\begin{bmatrix} 4l_e^2 & 13l_e & -3l_e^2 & 0 & 0 \\ 13l_e & 312 & 0 & 54 & -13l_e \\ -3l_e^2 & 0 & 8l_e^2 & 13l_e & -3l_e^2 \\ 0 & 54 & 13l_e & 156 & -22l_e \\ 0 & -13l_e & -3l_e^2 & -22l_e & 4l_e^2 \end{bmatrix}$$

$$\boldsymbol{K} = \frac{EI}{l_e^3}\begin{bmatrix} 4l_e^2 + k_r & -6l_e & 2l_e^2 & 0 & 0 & \\ -6l_e & 24 & 0 & -12 & 6l_e & \\ & 2l_e^2 & 0 & 8l_e^2 & -6l_e & 2l_e^2 \\ 0 & -12 & -6l_e & 12 & -6l_e & \\ 0 & 6l_e & 2l_e^2 & -6l_e & 4l_e^2 & \end{bmatrix}$$

The preceding equation leads to the following ordinary differential equation:

$$\boldsymbol{M}\ddot{\delta} + \boldsymbol{K}\delta = \boldsymbol{F(t)}, \qquad \delta = \begin{bmatrix} \theta_1 & w_2 & \theta_2 & w_3 & \theta_3 \end{bmatrix}^T$$

Where δ is a vector containing the nodal degrees of freedom w_i and θ_i at each node of the discrete element and $\boldsymbol{F(t)}$ is the global force vector.
To solve the system under an external time dependent force numerical integration scheme can be used and will be discussed later.

For free vibration where $\boldsymbol{F(t)}$ is zero is the natural frequencies and mode shape can be solved as an eigenvalue problem given as

$$\left[\boldsymbol{M} - \omega^2 \boldsymbol{K}\right]\delta = 0$$

In this ω will be the natural frequency and δ the corresponding mode shapes.

B.2. Finite element method to rotating beam

Consider the gangway is rotating similarly as shown in Figure 4.13. The Euler-Bernoulli beam theory was used to model the dynamic behavior of the gangway. Presume that the total displacement $z(y,t)$ of a point along the gangway at a distance y from its rotating base is function of the rigid body rotation $\phi(t)$ and the elastic deflection $w(y,t)$ measured from a the non rotating frame is given as

$$z(y,t) = y\varphi(t) + w(y,t) \tag{B.1}$$

Using finite element method to solve the dynamic problem leads to a equation

$$w(y,t) = \boldsymbol{d}(y)\delta(t) \tag{B.2}$$

where $\boldsymbol{d}$ represents the shape functions, see Chapter 4.1, and δ are the nodal displacements.
Substituting Equation B.2 into Equation B.1 leads to the following simplified form:

$$z(y,t) = \boldsymbol{d_z}(y)\boldsymbol{\delta}(t)$$

In this the new shape function $\boldsymbol{d_z}$ and nodal displacements $\boldsymbol{\delta}$ is as follow:

$$\boldsymbol{d_z} = \begin{bmatrix} y & \boldsymbol{d} \end{bmatrix} \qquad \boldsymbol{\delta} = \begin{bmatrix} \varphi(t) \\ \delta \end{bmatrix}$$

The kinetic energy and strain energy of each element can be expressed as

$$E_{kin} = \frac{1}{2}\int_0^{l_e} \rho A(y)\left(\frac{\partial z}{\partial t}\right)^2 dy \qquad E_{pot} = \int_0^{l_e} EI(y)\left(\frac{\partial^2 z}{\partial y^2}\right)^2 dy$$

Again using the procedure discussed in Chapter 4.1, the element mass and stiffness matrix can be obtained as:

$$[M_{rot}] = \frac{\rho A l_e}{420} \begin{bmatrix} m_1 & m_{12} & m_{13} & m_{14} & m_{15} \\ m_{12} & 156 & 22l_e & 54 & -13l_e \\ m_{13} & 22l_e & 4l_e^2 & 13l_e & -3l_e^2 \\ m_{14} & 54 & 13l_e & 156 & -22l_e \\ m_{15} & -13l_e & -3l_e^2 & -22l_e & 4l_e^2 \end{bmatrix} \tag{B.3}$$

$$[K_{rot}] = \frac{EI}{l_e^3} \begin{bmatrix} 0 & 0 & 0 & 0 & 0 \\ 0 & 12 & 6l_e & -12 & 6l_e \\ 0 & 6l_e & 4l_e^2 & -6l_e & 2l_e^2 \\ 0 & -12 & -6l_e & 12 & -6l_e \\ 0 & 6l_e & 2l_e^2 & -6l_e & 4l_e^2 \end{bmatrix} \tag{B.4}$$

where

$$\begin{aligned} m_1 &= 140l_e^2\left(3n^2 - 3n + 1\right) \\ m_{12} &= 21l_e\left(10n - 7\right) \\ m_{13} &= 7l_e^2\left(5n - 3\right) \\ m_{14} &= 21l_e\left(10n - 3\right) \\ m_{15} &= -7l_e^2\left(5n - 2\right) \end{aligned}$$

and n denotes the number of elements used.

B.3. Finite element to axial translating beam

Consider a beam translating axially under a constant velocity U. The equation of motion describing an axially translating beam are discussed in Chapter 4.4.3. The forumlation of the axial translating beam using finite element method will not be discussed here, for reference see [13]. The ordinary differential equation describing an axial translating beam neglecting the material in finite element takes the form:

$$\boldsymbol{M}\ddot{\delta} + \boldsymbol{C_T}\dot{\delta} + (\boldsymbol{K} + \boldsymbol{K_T})\,\delta = 0$$

Where $\boldsymbol{M}$ and $\boldsymbol{K}$ are the convention mass stiffness matrix that has been described previously.
The transport matrices $\boldsymbol{C_T}$ and $\boldsymbol{K_T}$ are given as

$$\boldsymbol{C_T} = \frac{\rho A U}{30} \begin{bmatrix} 0 & 6l_e & 30 & -6l_e \\ -6l_e & 0 & 6l_e & -l_e^2 \\ -30 & -6l_e & 0 & 6l_e \\ 6l_e & l_e^2 & -6l_e & 0 \end{bmatrix} \tag{B.5}$$

$$\boldsymbol{K_T} = -\frac{\rho AU^2}{30l_e}\begin{bmatrix} 36 & 3l_e & -36 & 3l_e \\ 3l_e & 4l_e^2 & -3l_e & 2l_e^2 \\ -36 & -3l_e & 36 & -3l_e \\ 3l_e & -l_e^2 & -3l_e & 4l_e^2 \end{bmatrix} \tag{B.6}$$

B.4. Numerical time integration

a numerical time integration scheme is used to solve the ordinary differential equation with its initial condition. As discussed the finite element method is used to discretize the beam in space domain.
There exist several integration scheme to solve the second order differential equation. During analysis in this thesis two types of integration scheme were used.
The first one being the '**ODE45**', this is a build in function in MATLAB that adopts the Runge-Kutta method. and the second one being the **Newmark-β** method.

Newmark-β algorithm

Using **Newmark-β** to solve the first derivative of the second differential equation in time, NEWMARK proposes two parameters γ and β to determine to position δ and velocities $\dot{\delta}$ at a forward time step $t+\Delta t$. The algorithm to implement Newmark-β method for direct integration is summed up as follow:

1. Initialize the initial condition for the displacement δ_0, velocity $\dot{\delta_0}$ and acceleration $\ddot{\delta_0}$
2. Form the effective matrix $\tilde{\boldsymbol{K}}$

$$\tilde{\boldsymbol{K}} = \boldsymbol{K} + a_0\boldsymbol{M} + a_1\boldsymbol{C}$$

3. At each forward time step calculate the effective loading $\tilde{\boldsymbol{F}}$

$$\tilde{\boldsymbol{F}} = \boldsymbol{F_{t+\Delta t}} + \boldsymbol{M}\left(a_0\delta_t + a_2\dot{\delta}_t + a_3\ddot{\delta}_t\right) + \boldsymbol{C}\left(a_1\delta_t + a_4\dot{\delta}_t + a_5\ddot{\delta}_t\right)$$

4. Determine the displacement at the next time step using

$$\tilde{\boldsymbol{K}}\delta_{t+\Delta t} = \tilde{\boldsymbol{F}}$$

5. Determine the acceleration and velocity at each each forward time step with the known displacement using

$$\ddot{\delta}_{t+\Delta t} = a_0\left(\delta_{t+\Delta t} - \delta_t\right) - a_2\dot{\delta}_t - a_3\ddot{\delta}_t$$

$$\dot{\delta}_{t+\Delta t} = \dot{\delta}_t + a_6\ddot{\delta}_t + a_7\ddot{\delta}_{t+\Delta t}$$

The integration constant $a_0..a_7$ are given as

$$a_0 = \frac{1}{\beta\Delta t^2}, \qquad a_1 = \frac{\gamma}{\beta\Delta t}, \qquad a_2 = \frac{1}{\beta\Delta t}, \qquad a_3 = \frac{1}{2\beta} - 1$$

$$a_4 = \frac{\gamma}{\beta} - 1, \qquad a_5 = \frac{\Delta t}{2}\left(\frac{\gamma}{\beta} - 2\right), \qquad a_6 = \Delta t\left(1-\gamma\right), \qquad a_7 = \gamma\Delta t$$

The obtain the solution the NEWMARK parameters β and γ needs to be chosen. By default the values of $\beta = \frac{1}{4}$ and $\gamma = \frac{1}{2}$. Choosing this value leads to a so called 'constant acceleration method [5].

C

Additional Dynamic Response

In this section additional dynamics response to external disturbance are given.

C.1. Gangway response to free floating drift away

In free floating mode, the gangway moves along with the residual motion of the hexapod. During this stage the gangway pushes a constant telescoping force to the platform to ensure that the gangway is still attached to the structure if by any means the ship drift away from its position. When the vessel moves towards the platform, the movable T-boom will be pushed inwards and vice versa.
A sudden drift away of the ship can be so large that the gangway no longer is attach to the offshore platform. The luffing cylinder is designed to counteract the dead weight of the gangway, so that the gangway stays in its position when a sudden drift away occurs. Most of the time those incidence occur along with a person standing on the gangway. The luffing cylinder cannot cope with both the weight of the person and the gangway will bounce back to its neutral/equilibrium position, causing a vertical bending vibration due to the weight of the person.

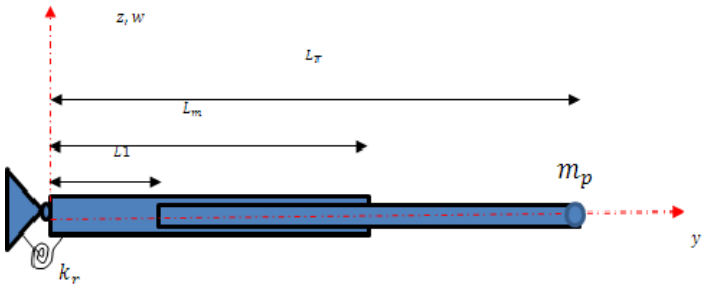

Figure C.1: Free floating drift away

a graphical representation can be seen in Figure C.1 and the equation motion written in general to describe the response is as follow:

$$\rho A \frac{\partial^2 w(x,t)}{\partial t^2} + \frac{\partial^2}{\partial x^2}\left(EI\frac{\partial^2 w(x,t)}{\partial x^2}\right) = m_p g \delta(y-L) \tag{C.1}$$

In this m_p denotes the mass of a person, g is the gravity and L is a variable length. The tip displacement time response is given in Figure C.2.

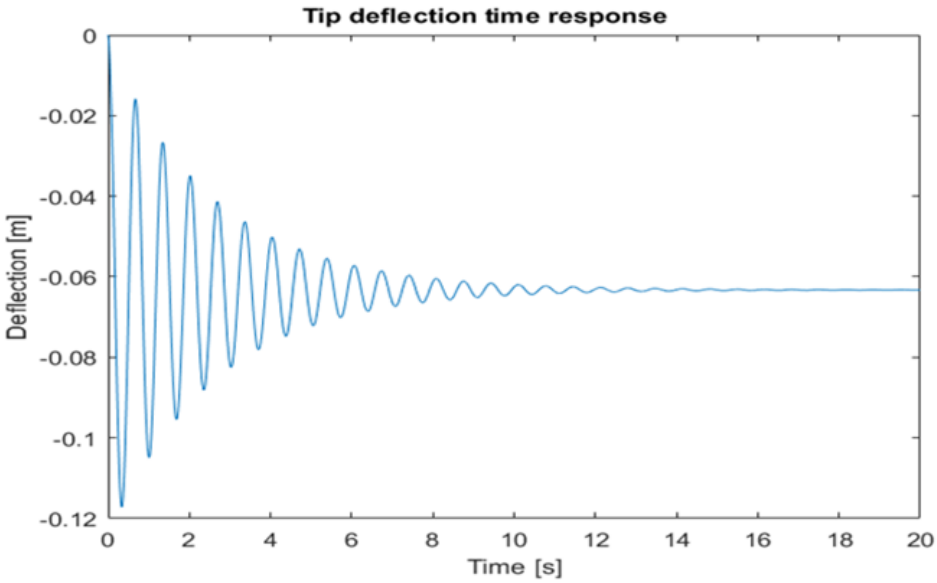

Figure C.2: Time response to drift away

D

Rainflow Cyclic Counting

An example of how to perform the rainflow cyclic counting technique on a simplified stress time history is shown. It should be noted that the stress time history given serve as an example and it does not represent the stress time history from this thesis.
Consider a stress time history given as in Figure D.1.

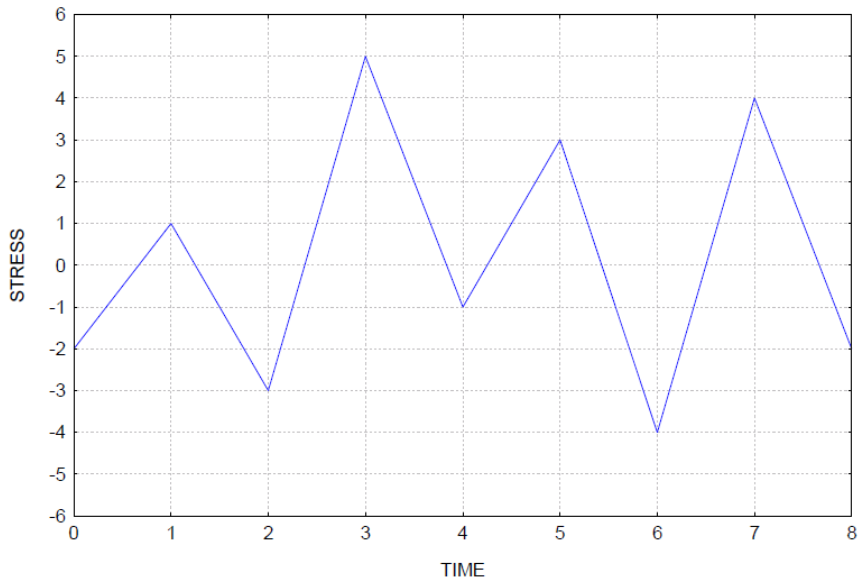

Figure D.1: Stress time history [[11]].

To count the number of stress cycle first one need to rotate the stress time plot and draw rainflows dripping from each roof and is illustrated in Figure D.2. The stress cycle range is counted by performing the following rules:

1. The flow starts from each peak.

2. The flow started from a peak continues to flow down and terminates when the magnitude of the following peak is equal or larger than the previous peak.

3. The flow stops when it intercepts with the previous flow from above.

Applying the rules to count the number of cycles of each stress range, the results are given in Table D.1.

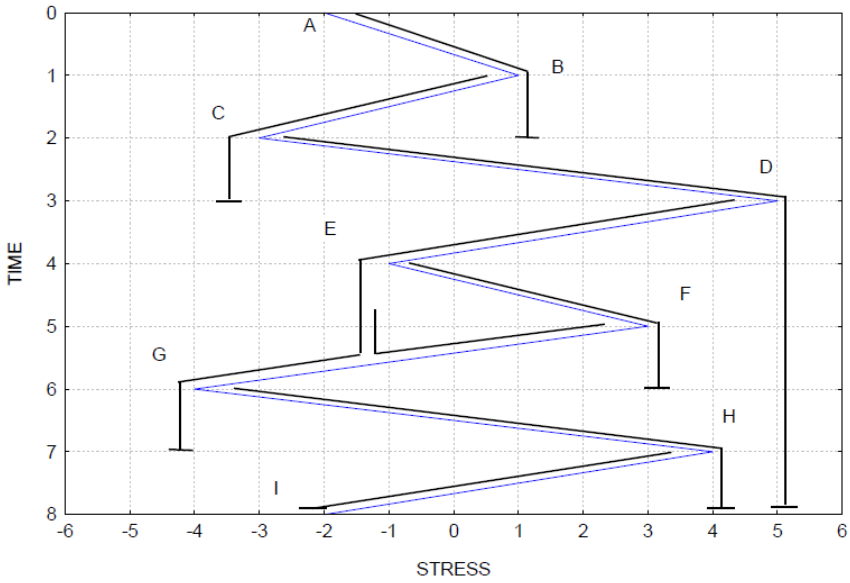

Figure D.2: Rainflow cycles illustation [[11]].

Table D.1: Rainflow cycle count

From	**To**	**From**	**To**	**Range**	**Cycle**
A	B	-2	1	3	0.5
B	C	1	-3	4	0.5
C	D	-3	5	8	0.5
D	G	5	-4	9	0.5
E	F	-1	3	4	1
G	H	-4	4	8	0.5
H	I	4	-2	6	0.5

Every stress range path is counted as half cycle. However, path E-F is counted as one cycle, because some of the flow is considered also in F-G.
The ASTM standard [1] gives a computer algorithm that performs the rainflow cyclic counting which is used in this thesis to perform the analysis.

Bibliography

[1] Astm e1049-85(2011)e1, standard practices for cycle counting in fatigue analysis. Journal article, 2011.

[2] DET NORSKE VERITAS AS. Dnv-rp-c203 fatigue design of offshore steel structures. Report, 2011.

[3] DET NORSKE VERITAS AS. Dnv-os-j101 design of offshore wind turbine structures. Report, 2014.

[4] Y. I. Kim B. Tabarrok, C. M. Leech. On the dynamics of an axially moving beam.

[5] K. J. Bathe. *Finite Element Procedures*. Prentice-Hall, Inc, New Jersey, 1996.

[6] J. T. Broch. *Mechanical Vibration and Shock Measurement*. Brüel and Kjaer, Denmark, 1984.

[7] Shu-Chyuarn Lin Chung-Feng Jeffrey Kuo. Discretization and computer simulation of a rotating euler–bernoulli beam. *Mathematics and Computers in Simulation*, 52, 2000.

[8] C.W. de Silva. *Vibration: Fundamentals and Practice, Second Edition*. Taylor & Francis, 2006. ISBN 9781439858158.

[9] F. Marazzi F. Casciati, G. Magonette. *Technology of Semiactive Devices and Applications in Vibration Mitigation*. John Wiley & Sons, Ltd, 2006.

[10] J. Chung H. Kim, H. H. Yoo. Dynamic model for free vibration and response analysis of rotating beams. *Journal of Sound and Vibration*, 332:5917–5928, 2013.

[11] Tom Irvine. Rainflow cycle counting in fatigue analysis. Report, 2011.

[12] E.C. Klaver J.M.J Spijkers, A.W.C.M. Vrouwenvelder. *Structural Dynamics part 1-Structural vibration*. 2005.

[13] Usik Lee. *Spectral Element Method in Structural Dynamics*. John Wiley & Sons, Ltd, Singapore, 2009.

[14] A.V. Metrikine. *Dynamics, Slender Structures and an Introduction to Continuum Mechanics CT 4145*.

[15] Ampelmann Operation. Basis of design ampelmann a-20-xl-ogw. Report.

[16] A.G. Verweij. *Markerless Position Measurement for Ship to Ship Transfer Operations*. Thesis, 2014.

[17] V.Z. Vlasov. *Thin-Walled Elastic Beam*. 1961.

[18] Hong-Tae Kang Yung-Li Lee, Mark E.Barkey. *Metal Fatigue Analysis Handbook*. Butterworth-Heinemann, 2012.